JCB Journal of Cell Biology

ARTICLE

VAMP4 regulates insulin levels by targeting secretory granules to lysosomes

Min Li[1,2,5,6], Fengping Feng[1], Han Feng[1], Pengkai Hu[1,4], Yanhong Xue[1], Tao Xu[1,2,3,4], and Eli Song[1,4]

Insulin levels are essential for the maintenance of glucose homeostasis, and deviations lead to pathoglycemia or diabetes. However, the metabolic mechanism controlling insulin quantity and quality is poorly understood. In pancreatic β cells, insulin homeostasis and release are tightly governed by insulin secretory granule (ISG) trafficking, but the required regulators and mechanisms are largely unknown. Here, we identified that VAMP4 controlled the insulin levels in response to glucose challenge. VAMP4 deficiency led to increased blood insulin levels and hyperresponsiveness to glucose. In β cells, VAMP4 is packaged into immature ISGs (iISGs) at trans-Golgi networks and subsequently resorted to clathrin-coated vesicles during granule maturation. VAMP4-positive iISGs and resorted vesicles then fuse with lysosomes facilitated by a SNARE complex consisting of VAMP4, STX7, STX8, and VTI1B, which ensures the breakdown of excess (pro)insulin and obsolete materials and thus maintenance of intracellular insulin homeostasis. Thus, VAMP4 is a key factor regulating the insulin levels and a potential target for the treatment of diabetes.

Introduction

Insulin is a key hormone responsible for the maintenance of glucose homeostasis, and aberrant variations in the insulin levels are believed to cause pathoglycemia or diabetes (Rorsman and Braun, 2013). In insulin-producing and insulin-releasing pancreatic β cells, the insulin amount is balanced by the biosynthesis, degradation, and secretion of insulin (Campbell and Newgard, 2021; Uchizono et al., 2007; Wicksteed et al., 2003), and the last two processes are achieved by intracellular trafficking of insulin secretory granules (ISGs; Hou et al., 2009; Vakilian et al., 2019). ISGs are derived from TGNs, where newly produced proinsulin and other cargoes are packaged into immature ISGs (iISGs; Davidson, 2004; Steiner et al., 2009), and iISGs then undergo a maturation process and transition to mature ISGs (mISGs) ready to release insulin upon stimulation (Howell and Bird, 1989; Suckale and Solimena, 2010). The maturation process involves multiple steps and is essential for the insulin quantity and quality. During maturation, iISGs are gradually acidified, resulting in the cleavage of proinsulin into mature insulin and C-peptide by prohormone convertases (Cheng et al., 2015; Malide et al., 1995; Martin et al., 1994; Naggert et al., 1995; Orci et al., 1986); to refine their granule size and contents, iISGs undergo a series of dynamic and complicated membrane remodeling processes, including homotypic fusion and resorting of undesired materials in a clathrin-coated vesicle (CCV)–dependent manner (Arvan and Castle, 1998; Du et al., 2016; Turner and Arvan, 2000; Wendler et al., 2001); and to maintain the optimal number of granules, some iISGs directly fuse with lysosomes for degradation (Rorsman and Renstrom, 2003).

In β cells, the total insulin amount and the number of insulin granules are tightly governed in response to physiological demands (Hinke et al., 2004; Rorsman and Renstrom, 2003). To maintain intracellular insulin homeostasis and ensure precise insulin release, excess (pro)insulin is packaged into iISGs and delivered to lysosomes for subcellular degradation via autophagy and/or crinophagy (Halban, 1991; Halban and Wollheim, 1980; Lee et al., 2019; Orci et al., 1984; Riahi et al., 2016; Schnell et al., 1988). Under normal conditions, crinophagy has been identified as a major pathway for direct fusion of secretory granules with lysosomes as a means of rapid elimination of unused secretory materials from the cytoplasm in multiple types of secretory cells, including exocrine, endocrine, and neuroendocrine cells (Csizmadia and Juhasz, 2020). Although crinophagy was described >50 yr ago (Smith and Farquhar, 1966), we

[1]National Laboratory of Biomacromolecules, CAS Center for Excellence in Biomacromolecules, Institute of Biophysics, Chinese Academy of Sciences, Beijing, China; [2]Guangzhou Laboratory, Guangzhou, China; [3]Shandong First Medical University and Shandong Academy of Medical Sciences, Jinan, China; [4]College of Life Sciences, University of Chinese Academy of Sciences, Beijing, China; [5]Bioland Laboratory (Guangzhou Regenerative Medicine and Health Guangdong Laboratory), Guangzhou, China; [6]Guangzhou Institutes of Biomedicine and Health, Chinese Academy of Sciences, Guangzhou, China.

Correspondence to Dr. Eli Song: songali@ibp.ac.cn; Dr. Tao Xu: xutao@ibp.ac.cn.

know little about this biological process. Particularly, in β cells the physiological significance of crinophagy remains unclear and the molecules that control this pathway are largely unknown. Rab7 interacting lysosome protein reportedly binds with ISG-associated Rab26 to direct ISGs for lysosomal degradation by interacting with lysosome-associated Rab7 (Zhou et al., 2020). Rab3 mutation in β cells enhances the lysosomal degradation of insulin granules (Marsh et al., 2007; Regazzi et al., 1996a; Yaekura et al., 2003). However, other protein machinery and molecular mechanisms required for crinophagy in β cells remain to be identified.

SNARE proteins play vital roles in mediating membrane fusion. The recognition of v-SNAREs on vesicles and t-SNAREs on the target membrane determines the specificity of membrane fusion (Chen and Scheller, 2001; Dingjan et al., 2018; McNew et al., 2000). Vesicle-associated membrane protein 4 (VAMP4), a v-SNARE protein, is predominantly located at TGNs and is also present on the plasma membrane, endosomes, and lysosome-related compartments (Rizzoli et al., 2006; Steegmaier et al., 1999; Tran et al., 2007). VAMP4 has been reported to participate in TGN-to-endosome anterograde transport via assembly with STX6 in PC12 cells (Steegmaier et al., 1999) and mediate endosome-to-TGN retrograde trafficking by complexing with STX16, VTI1A, and STX6 in nonsecretory cells (Hirata et al., 2015; Mallard et al., 2002), as well as controlling the probability of synaptic vesicle release via its targeting to endolysosomes in neurons (Ivanova et al., 2021). Additionally, VAMP4 is involved in the homotypic fusion of early endosomes by forming a SNARE complex with STX12, VTI1A, and STX6 and lipid droplet fusion by complexing with STX5 and SNAP23 (Bostrom et al., 2007; Brandhorst et al., 2006). In pituitary AtT-20 cells, VAMP4 is reportedly sorted from secretory granules along with synaptotagmin IV during membrane remodeling, as determined by biochemical experiments, and is proposed as a putative inhibitor of granule maturation (Eaton et al., 2000; Littleton et al., 1999). However, in pancreatic β cells, the dynamics, function, and molecular mechanism of VAMP4 involved in insulin granule trafficking and, in particular, the physiological roles of VAMP4 have not yet been clarified.

Here, using VAMP4 knockout mice, we revealed that VAMP4 deficiency causes increased insulin in the blood, accumulated intracellular (pro)insulin, and elevated insulin release in pancreatic β cells. Further experiments showed that VAMP4 localized to iISGs and was resorted to CCVs during granule maturation, and VAMP4-positive iISGs and resorted vesicles subsequently fused with lysosomes facilitated by a SNARE complex composed of VAMP4, syntaxin7 (STX7), syntaxin8 (STX8), and VTI1B on lysosomes. The fusion of iISGs with lysosomes promotes excess (pro)insulin degradation to control the intracellular insulin quantity and insulin release. The fusion of VAMP4-positive resorted vesicles with lysosomes degrades undesired granule cargoes, including prohormone convertase PC1 and PC2. Our data identified VAMP4 as a new regulator for controlling insulin levels and elucidated the molecular mechanisms of VAMP4 involved in insulin granule trafficking for the maintenance of intracellular insulin homeostasis in pancreatic β cells, providing the molecular basis that the absence of VAMP4 is beneficial for blood glucose control and that VAMP4 could be a potential target for the treatment of diabetes.

Results

VAMP4 KO mice exhibit hyperresponsiveness to glucose due to increased blood insulin

We generated a mouse model with global knockout of the *Vamp4* gene (hereafter named VAMP4 KO mice) using the CRISPR/Cas9 technique (Fig. 1 A). VAMP4 was completely deleted in islets and primary pancreatic β cells isolated from these KO mice (Fig. 1, B and C). The VAMP4 KO mice were viable and fertile and showed a slight nonsignificant reduction in body weight (Fig. 1 D), and no other obvious phenotypes with respect to feeding, mating performance, or overall behaviors were observed. Our analysis of the blood glucose profiles after the intraperitoneal administration of glucose revealed that male VAMP4 KO mice showed significantly enhanced glucose tolerance compared with the WT mice 15 min after high glucose stimulation (Fig. 1 E and Fig. S1 A), while the blood insulin level gradually increased in the KO mice and showed a significant increase 30 min after glucose administration (Fig. 1 F and Fig. S1 B). The VAMP4 KO mice performed normally in the insulin tolerance test (ITT; Fig. 1 G and Fig. S1 C) and exhibited normal random blood glucose (Fig. 1 H). These results indicate that VAMP4 KO mice exhibit hyperresponsiveness to glucose due to elevated blood insulin.

To explore the reasons for the increased release of insulin upon glucose stimulation in mice, we examined the pancreas and pancreatic islets of the VAMP4 KO mice. The morphology of the pancreas and the distribution and density of islets in the KO mice showed no obvious abnormalities (Fig. 2, A and C). The results from the quantification indicated that the area ratio of islets to the pancreas was slightly elevated in the KO mice (Fig. 2 D). The morphology and distribution of β cells and α cells inside islets were similar between the WT and KO mice (Fig. 2 B). Furthermore, the ratio of β cells to islet cells, the ratio of β cells to α cells, and the density of β cells or α cells in islets showed no significant difference between the WT and KO mice (Fig. 2, E–H). Interestingly, the mean levels of insulin were notably increased in the KO mice (Fig. 2 I), whereas the mean levels of glucagon showed no obvious difference between the two groups of mice (Fig. 2 J). These results suggest that the VAMP4 KO mice exhibit increased insulin levels in pancreatic β cells and unchanged glucagon levels in α cells.

VAMP4 deficiency causes increases in the intracellular (pro) insulin and insulin release

To validate the observed increase in the insulin levels in β cells and investigate why ablation of VAMP4 enhances the insulin levels at the body and cell levels, we used primary pancreatic β cells isolated from VAMP4 KO mice and VAMP4 gene-edited INS-1 cells to study the cellular mechanism. First, we analyzed the cellular distribution and expression of insulin and proinsulin in single primary β cells by immunofluorescence assays. Quantification revealed that the levels of proinsulin and insulin were 14% and 23% higher in the KO mice, respectively (Fig. 3, A–D). We then generated a *Vamp4* knockout (VAMP4

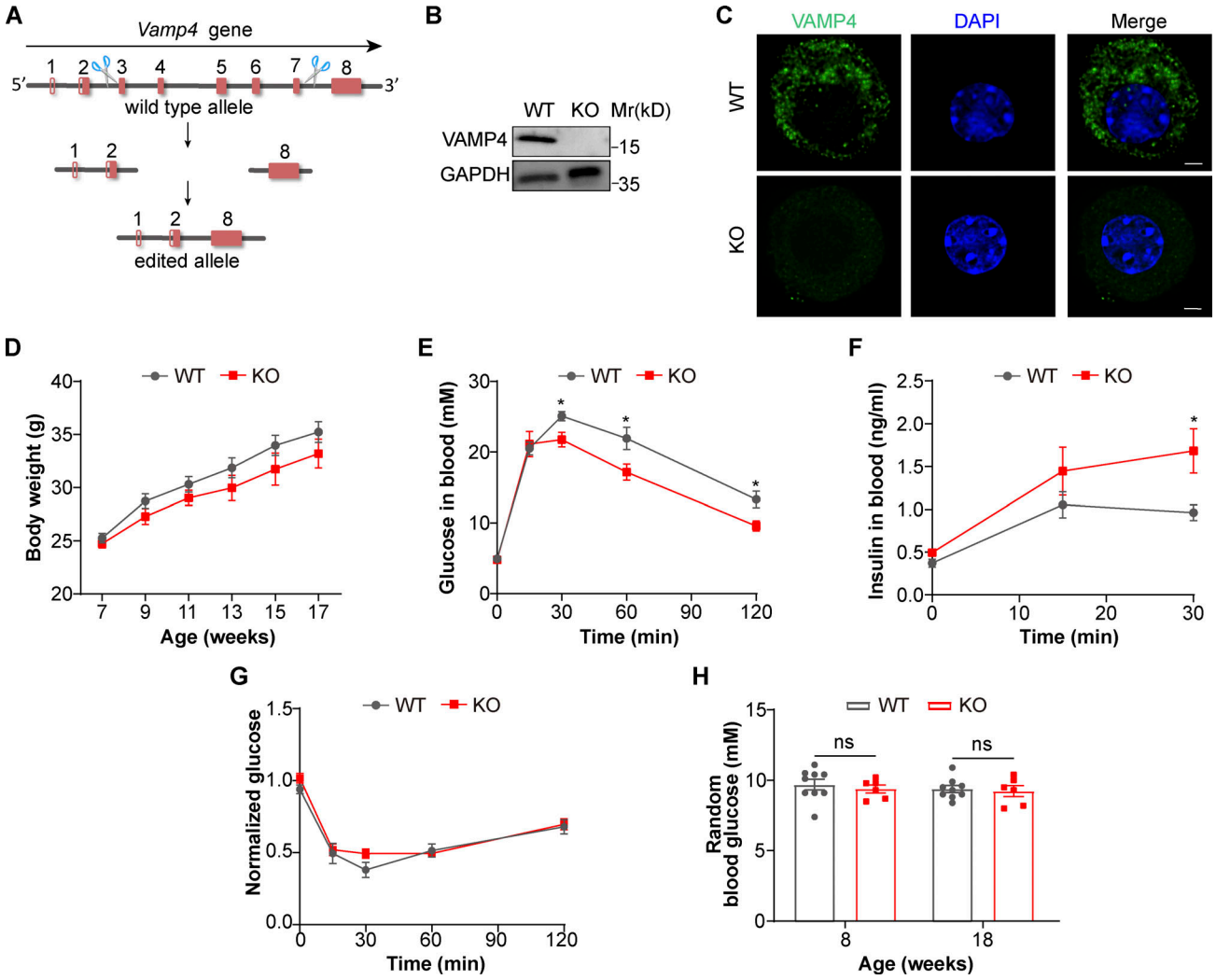

Figure 1. **VAMP4 KO mice exhibit hyperresponsiveness to glucose due to increased blood insulin levels. (A)** Schematic diagram of strategies for the generation of VAMP4 knockout mice, in which the region of *Vamp4* exon 3 to exon 7 was deleted, using the CRISPR/Cas9 technique. The solid bars represent ORFs, and the open bars represent UTRs. **(B)** Representative Western blot images showing the expression levels of VAMP4 in islets isolated from WT and KO mice (n = 3 biological independent samples). GAPDH was used as the loading control. 20 μg of protein was loaded in each lane. **(C)** Representative confocal images of VAMP4 staining (green) in primary β cells isolated from WT and KO mice (n = 3 biological independent samples). The nuclei of the cells were stained with DAPI (blue). Scale bars, 2 μm. **(D)** Body weight of male WT and KO mice (n = 6–9 mice per group). **(E and F)** GTT results (E) and blood insulin levels in the GTT (F) of male WT and KO mice at 14 wk of age for 2 g/kg body weight (n = 6–7 mice per group). **(G)** ITT results of male WT and KO mice at 16 wk of age for 0.5 U/kg body weight (n = 6–7 mice per group). **(H)** Ad libitum blood glucose in male WT and KO mice at the ages of 8 and 18 wk (n = 6–9 mice per group). The data are presented as the mean ± SEM. *, P < 0.05. The statistical analyses were performed with two-tailed unpaired Student's t test (D–H). Source data are available for this figure: SourceData F1.

KO) INS-1 cell line and a *Vamp4* knockdown (VAMP4 KD) INS-1 cell line using the CRISPR/Cas9 technique (Fig. S2, A–C). As determined by immunofluorescence staining of mixed cultured WT and VAMP4 KO INS-1 cells, proinsulin and insulin exhibited greater accumulation in the KO cells than in the WT cells (Fig. 3 E), and a fluorescence intensity analysis demonstrated that the proinsulin and insulin levels were 4.5-fold and 1.7-fold higher in the KO cells than in the WT cells, respectively (Fig. 3, F and G). Additionally, the ratio of proinsulin to total insulin (proinsulin and insulin) was significantly increased in the KO cells, indicating greater accumulation of immature proinsulin than mature insulin in the absence of VAMP4 (Fig. 3 H). Using ELISAs to accurately determine the intracellular amount of insulin and proinsulin, we obtained similar results: both the proinsulin and insulin levels were increased and the ratio of proinsulin to total insulin was elevated in the KO and KD cells compared with the WT cells (Fig. S2, D–F). We further rescued VAMP4 expression in the KO cells and observed that the increase in proinsulin and insulin exhibited efficient recovery (Fig. S2 G). To assess whether the increased insulin level is due to increased biosynthesis or reduced degradation, we detected the mRNA level of the *Ins* gene and observed no significant changes in the WT, KD, KO, and VAMP4 rescued INS-1 cells (Fig. S2 H), indicating that the increases in the amounts of insulin and proinsulin were due to diminished subcellular degradation rather than increased biosynthesis. These results indicate that VAMP4 deficiency increases the intracellular

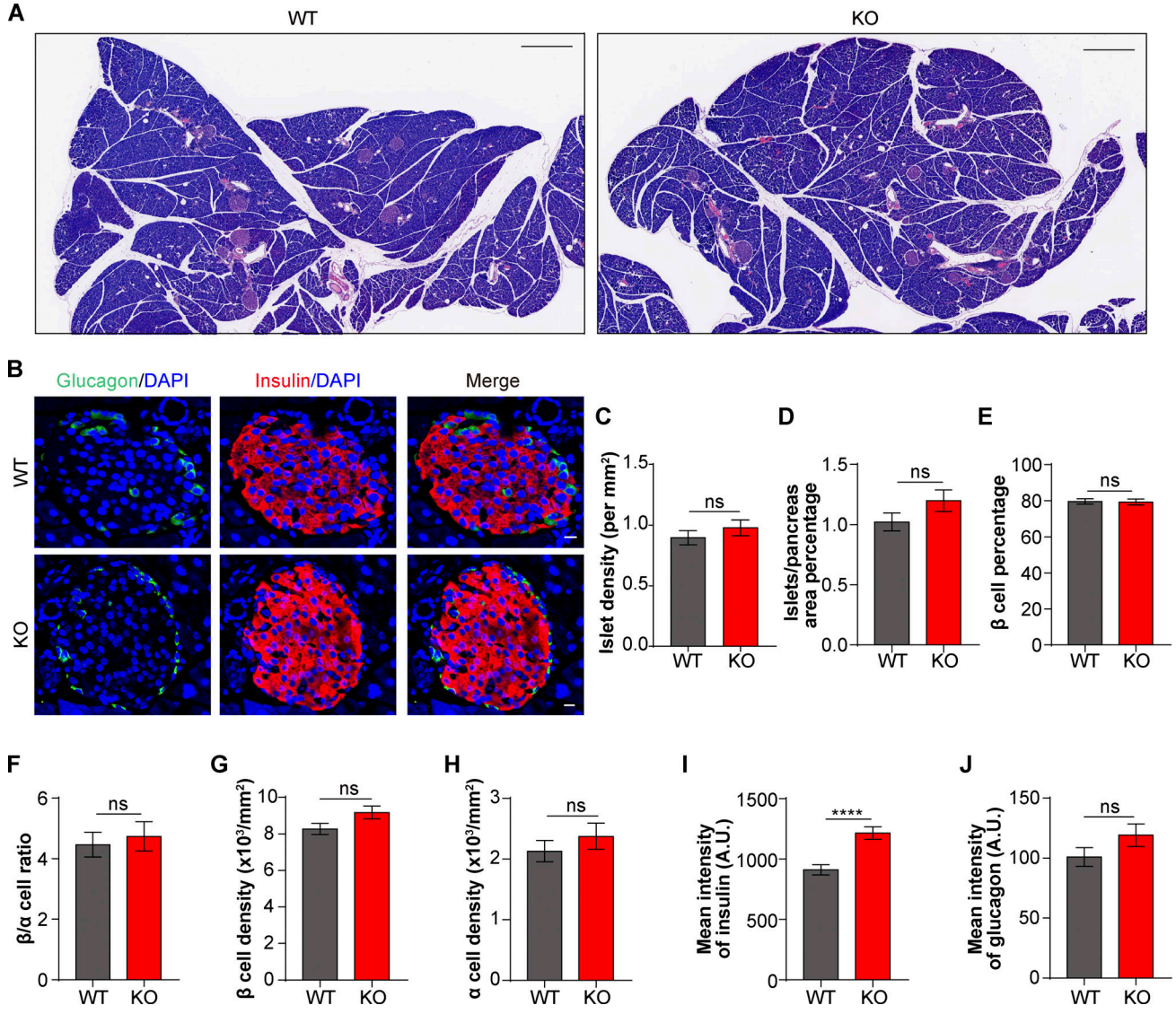

Figure 2. **VAMP4 KO mice show a normal pancreatic morphology but increased insulin levels. (A)** Representative H&E staining of the pancreas from WT and KO mice at 14 wk of age. Scale bars, 500 µm. **(B)** Representative confocal images of costaining for insulin (red) and glucagon (green) in islets isolated from WT and KO mice. The nuclei of cells were stained with DAPI (blue). Scale bars, 10 µm. **(C and D)** Islet-to-pancreas area percentage (D) and islet density in the pancreas (C) from WT and KO mice quantified by H&E staining of the pancreas shown in A. **(E–H)** The percentage of β cells among total cells (E), ratio of β cells to α cells (F), and density of β cells (G) and α cells (H) in islets from WT and KO mice were quantified by immunofluorescence staining, as shown in B. **(I and J)** Quantification of the mean fluorescence intensity of insulin (I) and glucagon (J) in islets from WT and KO mice based on the immunofluorescence staining results shown in B. The data used for the analysis in C–J were based on 20 islets counted per pancreas. *n* = 3, 1 female and 2 male mice at 14 wk of age. Immunofluorescence images were captured by confocal microscopy with a 40× (NA = 1.30) oil objective at room temperature. The data are presented as the mean ± SEM. ****, P < 0.0001. The statistical analyses were performed with two-tailed unpaired Student's *t* test (C–J).

amounts of proinsulin and insulin, specifically elevating the ratio of proinsulin to total insulin, which suggests that VAMP4 ablation leads to more proinsulin accumulation.

Next, we investigated whether the absence of VAMP4 changes the release of insulin. We performed a glucose-stimulated insulin secretion experiment to measure the insulin secreted from islets isolated from mice. The islets from VAMP4 KO mice released more insulin upon stimulation with either 2.8 or 16.7 mM glucose than WT islets (Fig. 3 I). Similar results were observed with VAMP4 KO and VAMP4 KD INS-1 cells, in which the amount of secreted insulin increased under low or high glucose stimulation, and the rescue of VAMP4 expression recovered this increase (Fig. 3 J and Fig. S2 I). These results indicate that VAMP4 ablation caused not only the accumulation of intracellular (pro)insulin but also an increase in insulin secretion.

VAMP4 deficiency results in increased PC1 and PC2 levels

To determine whether other granule cargoes show accumulation similar to (pro)insulin under VAMP4 deficiency, we assessed the amounts of PC1 and PC2, which are soluble granule cargoes packaged into iISGs at TGNs and are key prohormone convertases responsible for the conversion of proinsulin to insulin

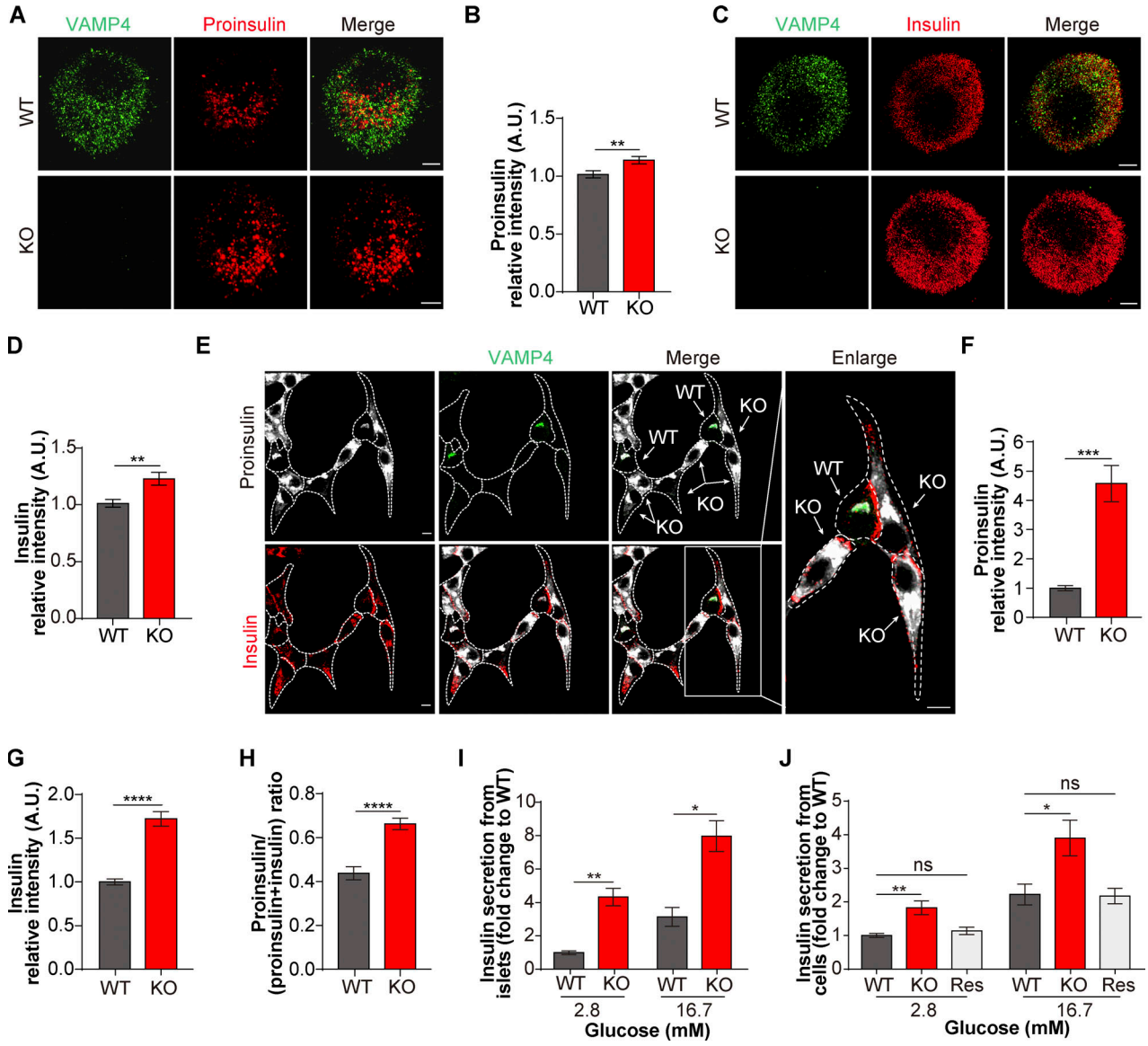

Figure 3. **VAMP4 deficiency causes increases in intracellular (pro)insulin and insulin release. (A–D)** Maximum intensity projection images showing the intensity of VAMP4 (green), proinsulin (red; A), and insulin (red; C) in β cells from WT and KO mice. Quantification of the proinsulin intensity (B) and insulin intensity (D) in whole cells based on the images shown in A and C. The data in B and D are shown as the mean ± SEM (n = 50 and 70 cells from four biological independent experiments, n = 4, 1 female and 3 male mice at 16 wk of age). Scale bars, 2 µm. **(E–H)** Representative confocal images costained for proinsulin (gray), insulin (red), and VAMP4 (green; E) in WT and KO INS-1 cells. The proinsulin intensity (F), insulin intensity (G), and ratio of proinsulin to total insulin (proinsulin and insulin; H) were quantified for maximum intensity projection based on the immunofluorescence staining data shown in E. Four sections of WT cells and five sections of KO cells were analyzed from three biological independent samples. Scale bars, 5 µm. **(I)** Measurement of insulin secretion from islets isolated from WT and KO mice incubated for 1 h in 2.8 or 16.7 mM glucose. 50 islets were used in each experiment, and three biological experiments were performed (n = 3, 1 female and 2 male mice at 16 wk of age). **(J)** Measurement of insulin secretion from WT, KO, and rescued INS-1 cells incubated for 1 h in 2.8 or 16.7 mM glucose (n = 6 biological independent samples). The data are presented as the mean ± SEM. *, P < 0.05; **, P < 0.01; ***, P < 0.001; and ****, P < 0.0001. The statistical analyses were performed with two-tailed unpaired Student's t test (B, D, and F–I) and one-way ANOVA (J).

(Cheng et al., 2015; Malide et al., 1995; Martin et al., 1994). Western blot results showed that the PC1 and PC2 levels are substantially increased in VAMP4-deficient cells, and the rescue of VAMP4 expression recovered the accumulation (Fig. 4, A–D). RT-PCR results showed that the mRNA levels of *Pc1* and *Pc2* exhibited no significant changes in WT, KD, KO, and VAMP4 rescued INS-1 cells (Fig. 4, E and F), which indicated that the increase in the PC1 and PC2 levels is due to their degradation rather than increased biosynthesis, similar to the results found for (pro)insulin. These results demonstrate that VAMP4 deficiency results in the accumulation of insulin granule cargoes, including both core cargoes, such as insulin and proinsulin, and soluble cargoes, such as PC1 and PC2.

No alterations of other VAMP proteins in the absence of VAMP4

VAMP4 is a member of the vesicle-associated membrane protein family, which has a similar structure and some of the members

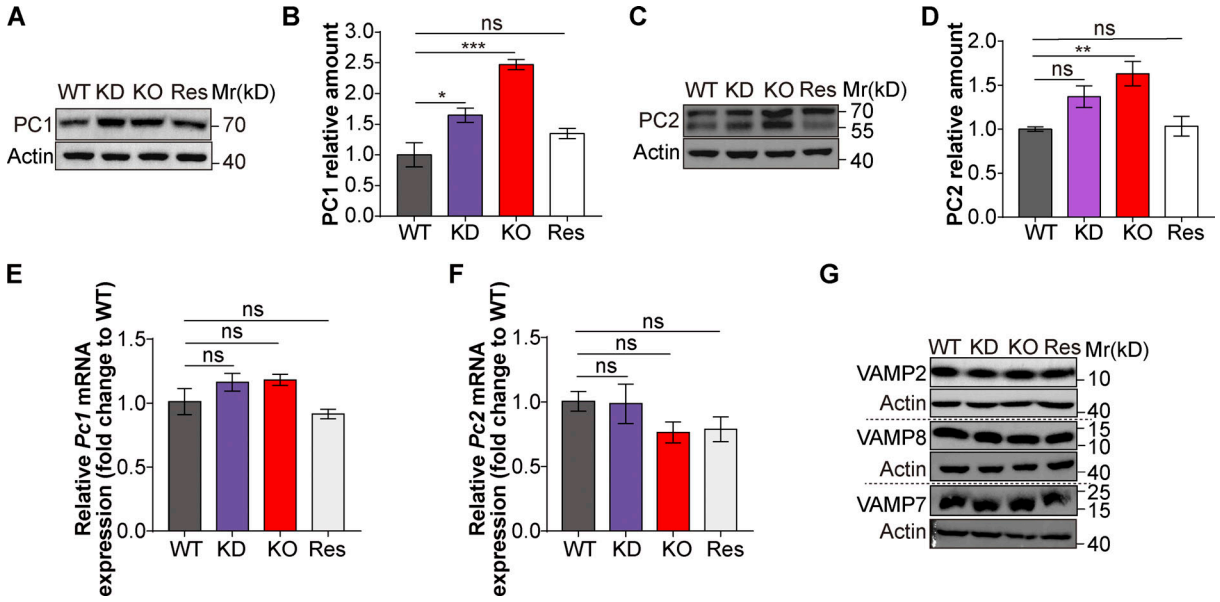

Figure 4. **VAMP4 deficiency leads to the accumulation of other granule cargoes. (A–D)** Representative Western blot images showing the expression levels of PC1 (A) and PC2 (C) in WT, KD, KO, and rescued INS-1 cells. The bar graphs show the expression levels of PC1 (B) and PC2 (D) quantified from three independent Western blot results. Actin was used as a loading control. **(E and F)** RT–PCR analysis of the *Pc1* (E) and *Pc2* (F) mRNA levels in WT, KD, KO, and rescued INS-1 cells. *18S* ribosomal RNA was used as an internal control (n = 3 biological independent experiments). **(G)** Representative Western blot images showing the expression levels of VAMP2, VAMP7, and VAMP8 in WT, KD, KO, and rescued INS-1 cells. Actin was used as the loading control. The data are presented as the mean ± SEM. *, P < 0.05; **, P < 0.01; and ***, P < 0.001. The statistical analyses were performed with one-way ANOVA (B and D–F). Source data are available for this figure: SourceData F4.

have an overlapping subcellular localization and execute similar functions (Advani et al., 1998; Feldmann et al., 2009). We wondered whether other VAMP proteins would be altered because of the VAMP4 deficiency. We performed Western blot experiments to determine the endogenous expression of several other VAMP proteins in VAMP4-deficient cells. No significant differences in the levels of VAMP2, VAMP7, and VAMP8 were observed in WT, KD, KO, and VAMP4 rescued INS-1 cells, indicating no obvious alterations of other VAMP proteins at the protein level (Fig. 4 G). Therefore, the abnormal phenotypes found for the VAMP4 KO mice or cells were specifically caused by the deletion of VAMP4.

VAMP4 localizes to iISGs and is resorted to CCVs during granule maturation

To investigate why VAMP4 deficiency results in the accumulation of granule cargoes and determine the molecular mechanism of VAMP4 involved in granule trafficking, we first examined the subcellular localization of VAMP4 in β cells. We used OptiPrep density gradient centrifugation to enrich ISGs and other organelles from INS-1 cells and analyzed the distribution of VAMP4 on different enriched fractions. The fractionation results showed that proinsulin was mainly distributed in fractions 2, 4, and 6, and insulin was increasingly expressed in fractions 6 and 8, which indicated that fractions 6 and 8 represented the iISG and mISG fractions, respectively (Fig. 5 A). Interestingly, VAMP4 was specifically distributed in fractions 2, 4, and 6 rather than fractions 8 and 10 (Fig. 5 A), indicating that VAMP4 localized to the early immature stages of ISGs and was not present in mature ISGs. The expression of PC1 and PC2 was also observed to be distributed mainly in fractions 2, 4, and 6 (Fig. 5 A), consistent with the findings from our previous ISG proteomic analysis (Li et al., 2018). The expression of PC1, PC2, and VAMP4 showed similar patterns in the cell fractions, suggesting that they have the same trafficking route during membrane remodeling in granule maturation. Collectively, these biochemical results indicate that VAMP4 localizes to iISGs and is absent in mISGs, which demonstrates the removal of VAMP4 from iISGs during granule maturation.

We then examined the dynamic subcellular localization of VAMP4 by live-cell imaging. Using EGFP-tagged VAMP4 and mCherry-tagged (pro)insulin to indicate VAMP4 and ISGs, we observed that in the TGN region, VAMP4 was mainly displayed on the surface of ISGs, and in peripheral regions, most VAMP4 was separate from ISGs (Fig. 5, B and C; and Fig. S3, A and B). iISGs are derived from TGNs and then are converted to mISGs during transport from the Golgi to the periphery. Thus, the live-cell imaging results suggested that VAMP4 localizes to iISGs but is absent in mISGs. Intriguingly, we noted a few events dynamically showing that VAMP4 was budded and removed from iISGs (Fig. 5 D and Video 1), and we also observed that VAMP4-positive iISGs were coated with clathrin (Fig. S3 C). During granule maturation, undesired granule cargoes are resorted to CCVs and removed from iISGs by membrane remodeling (Bonnemaison et al., 2013). We propose that VAMP4 is packaged into iISGs at TGNs and is subsequently resorted to CCVs and removed from iISGs during granule maturation.

VAMP4-positive iISGs and resorted vesicles fuse with lysosomes

To determine the trafficking destination of VAMP4-anchored vesicles, we tested the colocalization of VAMP4 with several

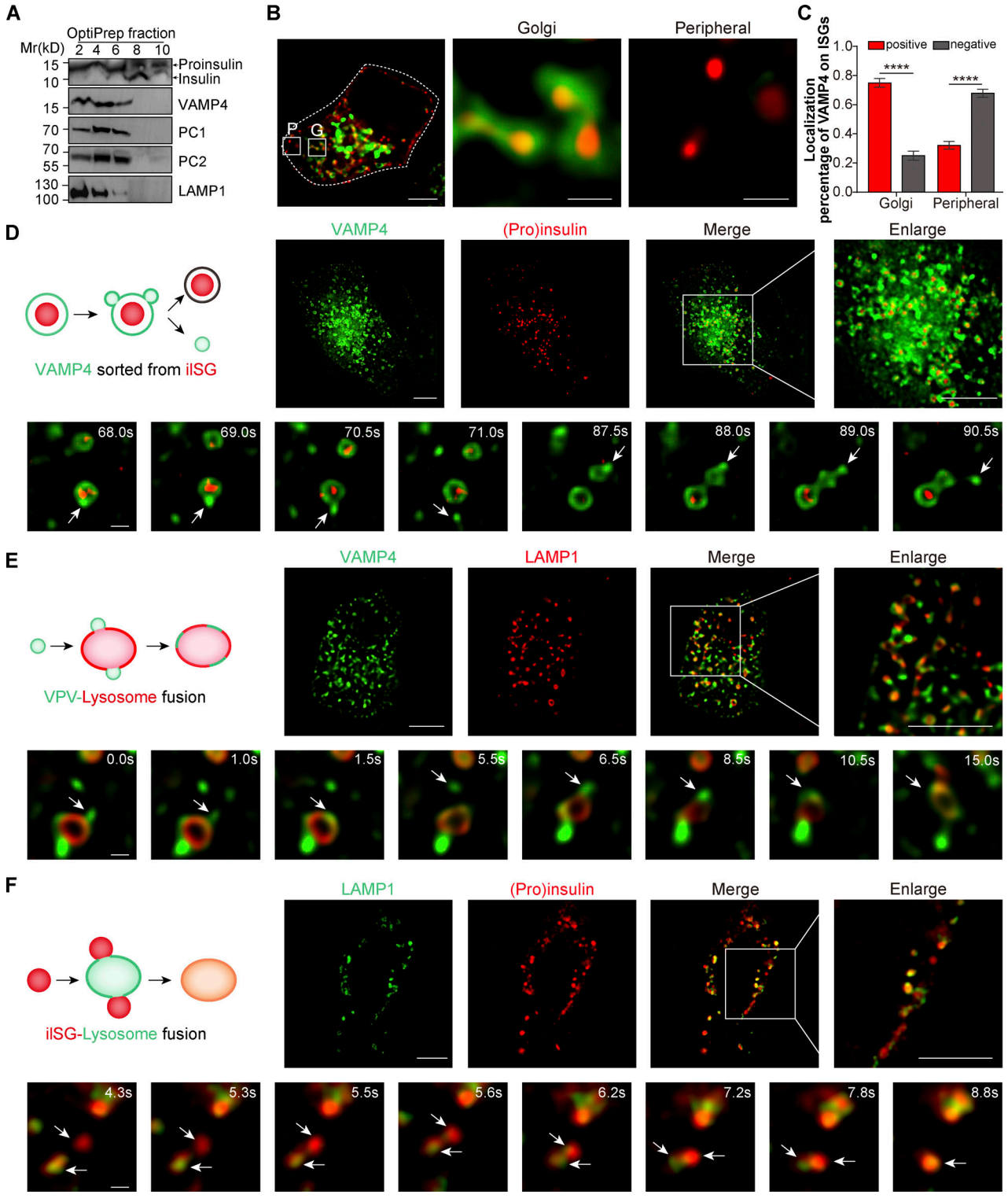

Figure 5. **VAMP4 localizes to iISGs and is resorted to CCVs during granule maturation, and VAMP4-positive iISGs and resorted vesicles fuse with lysosomes. (A)** Representative Western blot images showing the expression levels of proinsulin, insulin, VAMP4, PC1, PC2, and LAMP1 in different cellular fractions enriched by OptiPrep density gradient centrifugation (n = 3 biological independent experiments). **(B)** INS-1 cells were transfected with EGFP-tagged VAMP4 (green) and Halo-tagged (pro)insulin (red) plasmids for 48 h under live-cell imaging. Scale bars, 5 µm. Enlarged diagrams of the Golgi (G) region and peripheral (P) region are shown. Scale bars, 1 µm. **(C)** The percentage of VAMP4 localized on ISGs was higher in the Golgi region than in the peripheral region based on the three-dimensional live-cell imaging data shown in B (n = 6 sections of WT cells and KO cells from three independent experiments). The data are presented as the mean ± SEM. The statistical analyses were performed with two-way ANOVA. ****, P < 0.0001. **(D)** INS-1 cells were transfected with EGFP-tagged VAMP4 (green) and mCherry-tagged (pro)insulin (red) plasmids for 48 h under live-cell imaging. The diagram and a snapshot of a consecutive event showed that VAMP4 localized to the iISG surface and was removed from iISGs (indicated by arrows). **(E)** INS-1 cells were transfected with EGFP-tagged VAMP4

(green) and mCherry-tagged LAMP1 (red) plasmids for 48 h under live-cell imaging. The diagram and a snapshot of a consecutive event showed that VAMP4 fused with lysosomes and diffused on the lysosomal membrane (indicated by arrows), VPV, VAMP4-positive vesicle. **(F)** INS-1 cells were transfected with Halo-tagged LAMP1 (green) and mCherry-tagged (pro)insulin (red) plasmids for 48 h under live-cell imaging. The diagram and a snapshot of a consecutive event showed that (pro)insulin fused with lysosomes (indicated by arrows). Long-term live-cell imaging data were acquired using a Delta Vision OMX V3 system with 100× (NA = 1.40) in B and D–F. The data in D–F represent at least three biological independent experiments. Scale bars, 5 µm (D–F top) and 0.5 µm (D–F bottom). Source data are available for this figure: SourceData F5.

organelles in INS-1 cells by live-cell imaging. We observed that VAMP4 predominantly colocalized with lysosomes (Fig. 5 E). Notably, we observed a few dynamic events which showed VAMP4-labeled vesicles fused with LAMP1-labeled lysosomes and diffused on the lysosomal membrane (Fig. 5 E and Video 2). This result indicates that VAMP4-positive vesicles were transported to and fused with lysosomes. To investigate whether VAMP4-positive iISGs could be directly transported to lysosomes, we performed live-cell imaging and analyzed the colocalization of iISGs and lysosomes in INS-1 cells. We observed that VAMP4 coated (pro)insulin-labeled ISGs partially colocalized with lysosomes (Fig. 5 F and Fig. S3 D), and we captured a few dynamic events showing that ISGs directly fused with lysosomes (Fig. 5 F and Fig. S3 D and Video 3), indicating that VAMP4-positive iISGs can directly fuse with lysosomes. Thus, we demonstrated that both VAMP4-positive iISGs and resorted vesicles fuse with lysosomes.

VAMP4 interacts with STX7, STX8, and VTI1B to form a SNARE complex on lysosomes

Next, we deciphered the molecular mechanism as to how VAMP4 mediates the fusion of iISGs and resorted vesicles with lysosomes. As a v-SNARE, VAMP4 is supposed to spontaneously interact with t-SNAREs to form a SNARE complex mediating membrane fusion. To determine the VAMP4-associated t-SNAREs on lysosomes, we first performed a literature search for the t-SNAREs on lysosomes which belonged to the Qa, Qb, and Qc SNAREs and had the potential to be the binding partners of VAMP4 (Chen and Scheller, 2001; Dingjan et al., 2018; Feldmann et al., 2009; Kreykenbohm et al., 2002; Prekeris et al., 1999; Wang et al., 2017). Through preliminary exogenous immunoprecipitation (co-IP) experiments, we focused on STX7, STX8, and VTI1B. We then performed an in vitro GST pulldown assay to verify the binding ability of VAMP4, STX7, STX8, and VTI1B, and the results demonstrated that GST-tagged VAMP4 could pull down His-tagged STX7, STX8, and VTI1B (Fig. 6, A and B). We further carried out an endogenous co-IP experiment and identified that VAMP4, STX7, STX8, and VTI1B could precipitate the others (Fig. 6 C), indicating that they were all involved in a SNARE complex in vivo. If this SNARE complex mediates the fusion of VAMP4-anchored vesicles with lysosomes, it should localize to the lysosomal membrane. We detected the complex in isolated lysosomal fractions from INS-1 cells. The results demonstrated that VAMP4, STX7, STX8, and VTI1B were present in lysosomes (Fig. 6 D), and they could interact with each other and form a complex, as determined by a co-IP assay using lysosomal fractions (Fig. 6 E). These results indicated that VAMP4, STX7, STX8, and VTI1B form a SNARE complex on the lysosomal membrane.

To directly visualize the participation of VAMP4 in SNARE complex assembly in vivo, we employed live-cell imaging using the biomolecular fluorescence complementation (BiFC) approach. The fluorescence signal was generated by the complementation of nYFP-tagged VAMP4 and cYFP-tagged STX7 due to their close proximity via the interaction between VAMP4 and STX7. For the negative control, noncomplementation of nYFP-tagged VAMP4 and nYFP-tagged STX7 was observed (Fig. 6 F). Notably, complemented YFP signals induced by VAMP4 and STX7 showed good colocalization with LAMP1 or (pro)insulin, respectively. Additionally, we detected the interaction of VAMP4 with STX8 or VTI1B using the BiFC system and obtained similar results (Fig. 6, G and H). The fractionation experiment results also demonstrated that the distribution of VAMP4 and iISGs was highly consistent with that of lysosomes (Fig. 5 A). Altogether, these results provide direct evidence and demonstrate that VAMP4 associates with STX7, STX8, and VTI1B to assemble a SNARE complex on lysosomes, including the contact regions of insulin granules and lysosomes.

To further validate that VAMP4, STX7, STX8, and VTI1B functionally work together and that their formed SNARE complex is involved in the fusion of VAMP4-positive vesicles with lysosomes, we knocked down STX7 and STX8 individually and identified that a decrease in each of these proteins induces increased insulin release under either 2.8 or 16.7 mM glucose stimulation (Fig. S2, J–L), similar to the results found for VAMP4 KO cells (Fig. 3 J and Fig. S2 I). This result indicates that the SNARE complex consisting of VAMP4, STX7, STX8, and VTI1B is involved in maintenance of the insulin quantity.

VAMP4 facilitates the fusion of iISGs and resorted vesicles with lysosomes to mediate granule cargo degradation

To further examine whether the VAMP4-involved SNARE complex functionally contributes to the fusion of iISGs with lysosomes, we analyzed fusion events in primary β cells of WT and VAMP4 KO mice by EM. We observed that the number of ISGs per β cell increased, but the cytoplasmic area of β cells showed no significant change (Fig. 7 A; and Fig. S4, E and F); thus, the ISG density was markedly enhanced in the VAMP4 KO β cells (Fig. 7 C). We observed that the interaction between insulin granules and lysosomes involved multiple stages, including ISG-lysosome contact (Fig. 7 B I and Fig. S4 A), ISG-lysosome fusion (Fig. 7 B II and Fig. S4 B), ISG-lysosome engulfment (Fig. 7 B III and Fig. S4 C), and ISG-lysosome degradation (Fig. 7 B IV and Fig. S4 D). We analyzed the total events of ISG-lysosome interactions and found that the number and density of ISG-lysosome interactions were reduced (Fig. 7 D and Fig. S4 G) and that the ratio of ISG-lysosomes to total ISGs was substantially decreased in VAMP4 KO β cells (Fig. 7 E). Similarly, in

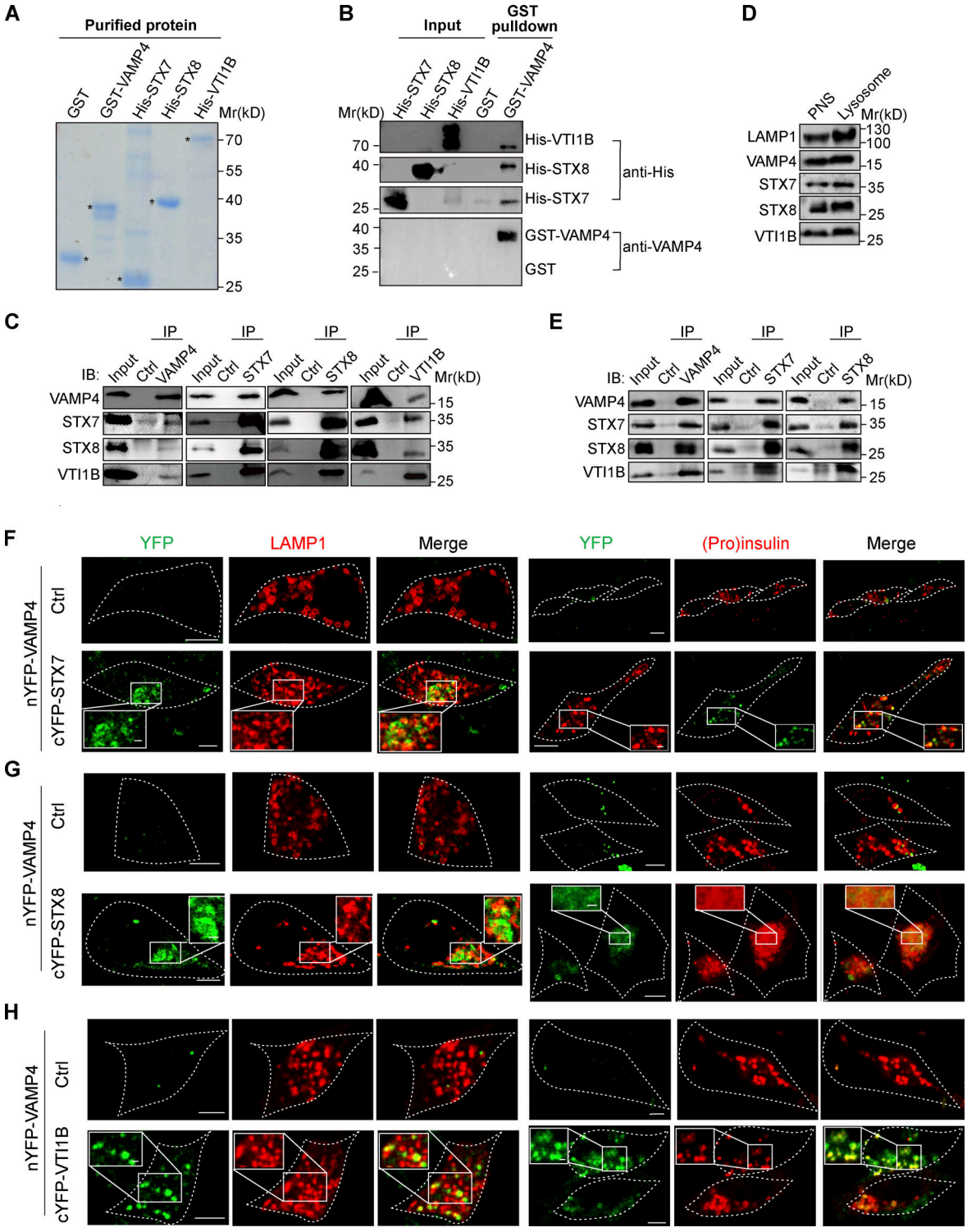

Figure 6. **VAMP4 interacts with STX7, STX8, and VTI1B to form a SNARE complex on lysosomes. (A)** GST and GST-tagged VAMP4 were purified by Glutathione Sepharose beads, and His-tagged STX7, STX8, and VTI1B were purified by Ni beads from *E. coli*. The purified proteins were determined by SDS–PAGE and Coomassie blue staining (n = 3 biological independent experiments). **(B)** Representative Western blot images showing the interaction of VAMP4 with STX7, STX8, and VTI1B determined by GST pulldown assay in vitro. His-tagged STX7, STX8, and VTI1B were immunoblotted (IB) with anti-His antibody, and GST and GST-tagged VAMP4 were immunoblotted with anti-VAMP4 antibody. GST protein was used as a negative control in the GST pulldown assay (n = 3 biological independent experiments). **(C)** The association of VAMP4, STX7, STX8, and VTI1B was detected by endogenous co-IP and immunoblotting with the indicated antibodies. IgG was used as a negative control in the co-IP assay. 3% of cell lysates and 10% of the immunoprecipitates were loaded (n = 4 biological independent experiments). **(D)** Representative Western blot images showing the expression levels of VAMP4, STX7, STX8, and VTI1B in the enriched lysosomal fraction. 15 µg of protein was loaded in each lane (n = 3 biological independent experiments). **(E)** The association of VAMP4, STX7, STX8, and VTI1B on lysosomes was detected by endogenous co-IP using enriched lysosomal fractions and immunoblotting with the indicated antibodies. IgG was used as a negative

control in the co-IP assay. 3% of the isolated lysosomal fraction and 10% of the immunoprecipitates were loaded (n = 3 biological independent experiments). **(F–H)** INS-1 cells were transfected with nYFP-tagged VAMP4, cYFP-tagged STX7, and nYFP-tagged STX7 (F), cYFP-tagged STX8 and nYFP-tagged STX8 (G), cYFP-tagged VTI1B and nYFP-tagged VTI1B (H), and mCherry-tagged LAMP1 and mCherry-tagged (pro)insulin plasmids for 48 h under live-cell imaging. The interaction of nYFP-tagged VAMP4 with cYFP-tagged STX7, cYFP-tagged STX8, or cYFP-tagged VTI1B was detected by BiFC assay. The plasmids of nYFP-tagged STX7, nYFP-tagged STX8, and nYFP-tagged VTI1B were used as a negative control. mCherry-tagged LAMP1 (red) and mCherry-tagged (pro)insulin (red) represent lysosomes and iISGs, respectively. Scale bars, 5 µm (F–H) and 1 µm (insets in F–H). Source data are available for this figure: SourceData F6.

VAMP4 KO INS-1 cells, the colocalization of ISGs with lysosomes was markedly decreased, as determined by live-cell fluorescent imaging (Fig. 7, F and G). These results clearly demonstrated that VAMP4 deficiency blocks the interaction and fusion of iISGs with lysosomes and causes the accumulation of insulin granules in cells, which strongly indicates that VAMP4 facilitates the membrane fusion of insulin granules with lysosomes and suggests that VAMP4 is a key regulator of the intracellular insulin granule number.

We speculate that the fusion of iISGs with lysosomes promotes the release of excess synthesized (pro)insulin into lysosomes for degradation and that the fusion of resorted vesicles with lysosomes results in the dumping of undesired materials into lysosomes for degradation. To test this hypothesis, we treated cells with chloroquine, a lysosomal inhibitor (Mauthe et al., 2018), and assessed the levels of intracellular proinsulin, VAMP4, PC1, and PC2. The results showed that the proinsulin, PC1 and PC2 levels, were increased in the WT and KO cells (Fig. 7 H), consistent with the above described results (Fig. 4, A–D and Fig. S2 G), and their levels increased with increases in the chloroquine treatment time (Fig. 7 H and Fig. S4, H–J). The rescue of VAMP4 expression in the KO cells reversed the increases in the proinsulin, PC1, and PC2 levels (Fig. 7 H and Fig. S4, H–J). These results indicated that the VAMP4 facilitated fusion of iISGs and resorted vesicles with lysosomes mediate the degradation of excess (pro)insulin to ensure maintenance of intracellular insulin homeostasis and regulate the degradation of undesired granule cargoes.

Discussion

Insulin is essential for the maintenance of body glucose homeostasis, and deviations from normal levels lead to diabetes (Roder et al., 2016). However, the cellular metabolic mechanism controlling the insulin quantity and quality has not been fully elucidated. In this study, we revealed a new regulator, VAMP4, which participated in the control of the insulin levels in pancreatic β cells, and elucidated the molecular mechanisms of VAMP4 involved in insulin granule trafficking for the maintenance of intracellular insulin homeostasis. Briefly, VAMP4 KO mice exhibit hyperresponsiveness to glucose due to increased blood insulin levels in response to glucose challenge. VAMP4-deficient pancreatic β cells show an accumulation of intracellular (pro)insulin, an increase in insulin release, and an elevated proportion of immature proinsulin. Mechanistically, in β cells VAMP4 is packaged into iISGs at TGNs and partial VAMP4-positive iISGs directly fuse with lysosomes via crinophagy. VAMP4 can also be resorted to CCVs and removed from iISGs by membrane remodeling during granule maturation, and VAMP4-positive resorted vesicles subsequently fuse with lysosomes. VAMP4 forms a SNARE complex with STX7, STX8, and VTI1B on lysosomes and promotes the membrane fusion of iISGs and resorted vesicles with lysosomes, ensuring the breakdown of excess (pro)insulin and obsolete materials to maintain intracellular insulin homeostasis (Fig. 7 I and Fig. S5).

We found that in pancreatic β cells, VAMP4 facilitates the fusion of iISGs with lysosomes via crinophagy. Crinophagy was discovered 50 yr ago by an electron microscopic examination of the lactotroph hormone-producing cells of the rat anterior pituitary gland (Smith and Farquhar, 1966). Since then, similar tightly regulated catabolic processes have been identified to regulate the secretory granule pool during the development of various types of secretory cells, particularly in exocrine, endocrine, and neuroendocrine cells (Csizmadia and Juhasz, 2020). However, the molecular mechanisms and physiological roles of crinophagy are largely unknown. Csizmadia et al. recently identified a SNAP receptor complex consisting of STX13, SNAP29, and VAMP7 that was required for the fusion of secretory granules with lysosomes in *Drosophila* salivary gland cells (Csizmadia et al., 2018). This study revealed that a SNARE complex composed of VAMP4, STX7, STX8, and VTI1B facilitated the membrane fusion of insulin granules with lysosomes in rodent pancreatic β cells. These results indicate that although crinophagy is a conserved pathway from *Drosophila* to metazoans, the protein machinery and molecular mechanisms required for the fusion of secretory granules and lysosomes in the crinophagy pathway in different cell types of different species are highly diverse and specific. Crinophagy is proposed to maintain the optimal insulin granule number and insulin homeostasis in β cells (Schnell et al., 1988). Our data demonstrate that the VAMP4 facilitated fusion of iISGs and resorted vesicles with lysosomes controlled the insulin quantity and quality in cells and in mice, providing direct evidence that crinophagy is related to whole-body glucose homeostasis. Hyperactive crinophagy in β cells is suggested to contribute to type 2 diabetes, which is characterized by insulin resistance, β cell dysfunction, and low insulin release (Pasquier et al., 2019; Weckman et al., 2014). We found that VAMP4 deficiency led to increases in the intracellular and blood insulin levels, indicating that the absence of VAMP4 is beneficial for blood glucose control and that VAMP4 may be a novel candidate for a therapeutic strategy to delay the onset or even prevent diabetes.

Previous studies from the Ricci group reported that under starvation conditions, nascent insulin granules were predominantly targeted to lysosomal degradation (termed starvation-induced nascent granule degradation [SINGD]), and macroautophagy was suppressed (Goginashvili et al., 2015; Pasquier et al., 2019). This process prevents insulin release under fasting conditions,

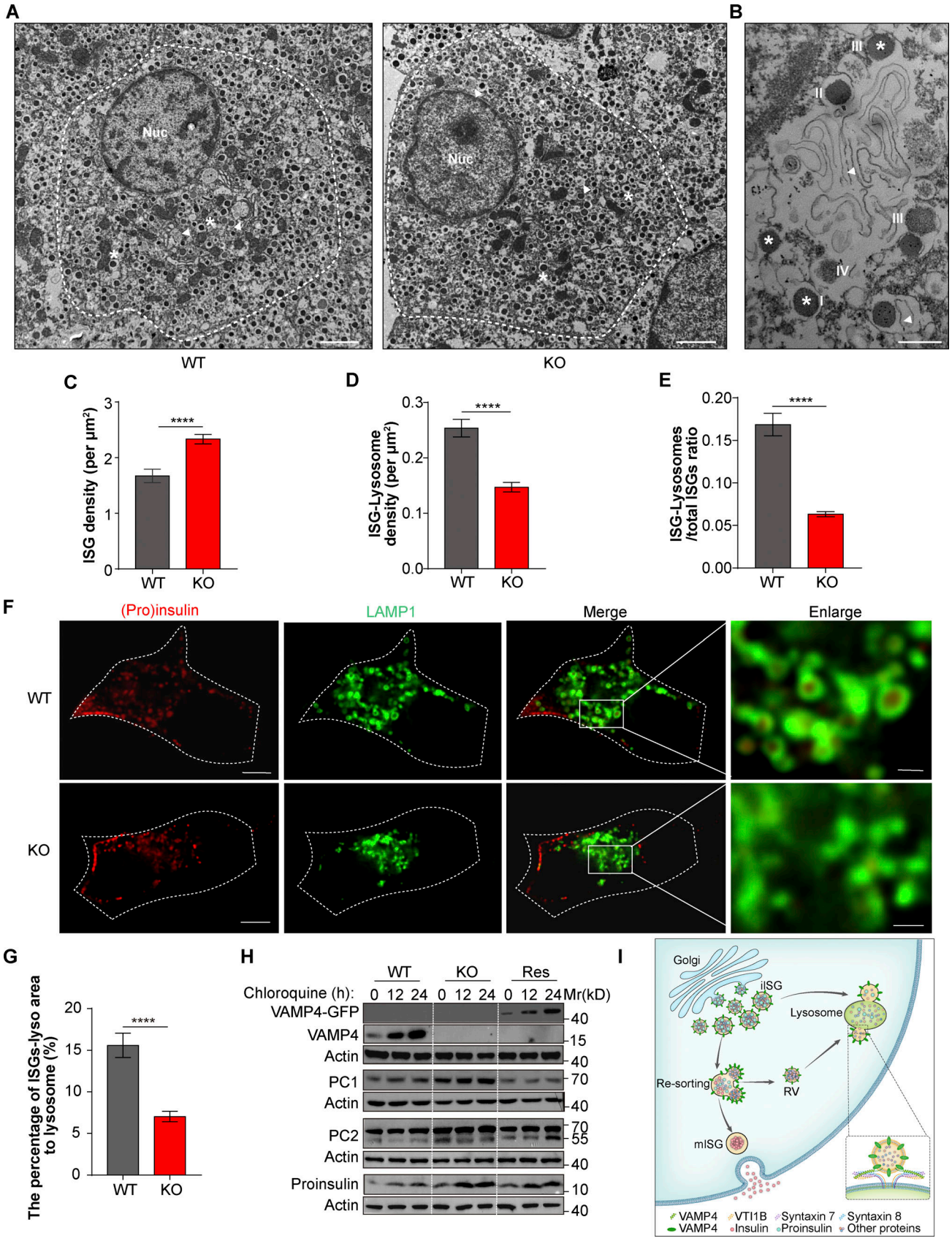

Figure 7. **VAMP4 facilitates the fusion of iISGs and resorted vesicles with lysosomes for granule cargo degradation. (A)** Representative EM images of pancreatic β cells from WT and KO mice were captured at 100 kV and a magnification of 4,800×. Triangle: lysosome; asterisk: ISG; Nuc: nuclei. Scale bars, 2 μm. **(B)** Region of interest in EM images of pancreatic β cells from WT mice showing that insulin granules and lysosomes exhibit multiple stages of interaction and

fusion. These stages include the following: (I) ISG-lysosome contact, (II) ISG-lysosome fusion, (III) ISG-lysosome engulfment, and (IV) ISG-lysosome degradation. Images were captured at 120 kV and a magnification of 23,000×. Triangle: lysosome; asterisk: ISG. Scale bars, 0.5 µm. **(C–E)** The ISG density (C), density of the ISG-lysosome interaction (D), and ratio of ISG-lysosome contact events to total ISGs (E) in WT and KO mice were quantified from the EM images shown in A. Events from all stages of the ISG-lysosome interaction were included. **(F)** WT and KO INS-1 cells were transfected with mCherry-tagged (pro)insulin (red) and Halo-tagged LAMP1 (green) for 48 h, and live-cell imaging was performed using the Delta Vision OMX V3 system with 100× (NA = 1.40). Scale bars, 5 µm (left) and 1 µm (right). **(G)** The bar graph showing the quantified colocalization of LAMP1 and (pro)insulin from the data in F. 10 sections of WT cells and 12 sections of KO cells were analyzed from three biological independent experiments. **(H)** Representative Western blot images showing the expression levels of VAMP4, PC1, PC2, and proinsulin in WT, KO, and rescued INS-1 cells treated with 100 µM chloroquine for 0, 12, and 24 h. Actin was used as a loading control. **(I)** VAMP4 working model. The data used for the analysis in C–E were based on 25 β cells in two islets isolated from one WT male mouse and 24 β cells in three islets isolated from two VAMP4 KO male mice. WT and VAMP4 KO mice were 16 wk of age. The data are presented as the mean ± SEM. ****, P < 0.0001. The statistical analyses were performed with two-tailed unpaired Student's *t* test (C–E and G). Source data are available for this figure: SourceData F7.

and the degradation of nascent insulin granules generates metabolites for cell survival to counter nutrient deprivation (Goginashvili et al., 2015; Pasquier et al., 2019). Our study demonstrates that under normal physiological conditions, partial iISGs that contain VAMP4 directly fuse with lysosomes for the degradation of excess (pro)insulin by forming a SNARE complex consisting of VAMP4 and STX7, STX8, and VTI1B on lysosomes. However, the function and molecular mechanism of VAMP4 under starvation conditions are unclear and need to be investigated in the future. Because SINGD is a special type of crinophagy, we propose that VAMP4 may have the same function in SINGD for the fusion of nascent insulin granules with lysosomes. Therefore, under starvation conditions, as more newly formed insulin granules fuse with lysosomes for degradation, VAMP4 deficiency would cause more prominent accumulation of insulin granules.

In cells, lysosomes act as a central degradation station by establishing membrane contact sites with other organelles to exchange contents (Lawrence and Zoncu, 2019; Luzio et al., 2007). The fusion selectivity and specificity of lysosomes with other organelles depend on the recognition of t-SNAREs on lysosomes and v-SNAREs on vesicles (Jena, 2011). In this study, we found that lysosomes fused with VAMP4-anchored iISGs and resorted vesicles, and other scientists previously reported that lysosomes fused with late endosomes mediated by VAMP7 and with autophagosomes facilitated by VAMP8 (Dingjan et al., 2018; Furuta et al., 2010; Pryor et al., 2004). After budding from TGNs, nascent iISGs contain multiple v-SNAREs, including VAMP2, VAMP3, VAMP4, VAMP7, and VAMP8 (Xiong et al., 2017). During granule maturation and membrane remodeling, different v-SNAREs are reorganized or resorted into different staged granules or vesicles, serving as the granule hallmark and determining the final destination of granule fusion. The newly formed iISGs and resorted vesicles contain VAMP4, which leads them to fuse with lysosomes by the VAMP4 recognition of t-SNAREs, STX7, STX8, and VTI1B on lysosomes. Mature ISGs contain VAMP2, which facilitates the fusion of mISGs with the plasma membrane by the VAMP2 recognition of SNAP25/23 and STX1A on the plasma membrane to release insulin (Eliasson et al., 2008; Regazzi et al., 1996b).

We not only identified the machinery involved in the fusion of iISGs with lysosomes, but also demonstrated that VAMP4 was resorted to CCVs from iISGs during granule maturation and VAMP4-positive resorted vesicles subsequently fused with lysosomes, which was also facilitated by the SNARE complex composed of VAMP4 and STX7, STX8, and VTI1B. The fusion of VAMP4-positive resorted vesicles with lysosomes promoted the degradation of resorted vesicles carrying nonsecretory or undesired materials, such as PC1 and PC2. VAMP4 deficiency led to abnormal accumulation of these undesired proteins. We also found that in VAMP4 KO β cells, although the levels of both proinsulin and insulin were increased, the ratio of proinsulin to total insulin was significantly elevated, which indicates greater accumulation of immature proinsulin than mature insulin, suggesting an imbalance in the intracellular insulin quantity and quality in the absence of VAMP4.

Material and methods

Antibodies and reagents

The following antibodies were used: rabbit anti-VAMP4 (Cat. no. 10738-1-AP; Proteintech), rabbit anti-STX8 (Cat. no. 12206-1-AP; Proteintech), rabbit anti-STX7 (Cat. no. 12322-1-AP; Proteintech), mouse anti-GAPDH (Cat. No. 60004-1-Ig; Proteintech), mouse anti-actin (Cat. No. 66009-1-Ig; Proteintech), rabbit anti-glucagon (Cat. no. 15954-1-AP; Proteintech), goat anti-mouse IgG HRP conjugate (Cat. no. SA00001-1; Proteintech), goat anti-rabbit IgG HRP conjugate (Cat. no. SA00001-2; Proteintech), rabbit anti-PC2 (Cat. no. 10553-1-AP; Proteintech), rabbit anti-PC1 (Cat. no. ab220363; Abcam), rabbit anti-VTI1B (Cat. no. ab184170; Abcam), rabbit anti-VAMP2 (Cat. no. ab181869; Abcam), rabbit anti-VAMP8 (Cat. no. ab76021; Abcam), rabbit anti-insulin (Cat. no. ab181547; Abcam), rabbit anti-VAMP7 (Cat. no. TA319712; OriGene), mouse anti-LAMP1 (Cat. no. MA1-164; Thermo Fisher Scientific), mouse anti-proinsulin (Cat. no. 2PR8-CCl-17; HyTest), mouse anti-insulin (Cat. no. 8138; Cell Signaling Technology), mouse anti-His Tag (Cat. no. YM3004; ImmunoWay), Alexa Fluor 405 goat anti-mouse (Cat. no. A-31553; Thermo Fisher Scientific), Alexa Fluor 488 goat anti-rabbit (Cat. no. A-11008; Thermo Fisher Scientific), Alexa Fluor 568 goat anti-mouse (Cat. no. A-11031; Thermo Fisher Scientific), Alexa Fluor 647 donkey anti-mouse (Cat. no. A-31571; Thermo Fisher Scientific), Janelia Fluor 646 HaloTag ligands (Cat. no. GA1110; Promega), and goat anti-guinea pig IgG, TRITC (Cat. no. 106-025-003; Jackson). The following reagents were used: RPMI 1640 medium (Cat. no. C22400500BT; Thermo Fisher Scientific), FBS (Cat. no. 10091148; Thermo Fisher Scientific), trypsin-EDTA (Cat. no. 25300054; Thermo Fisher Scientific), penicillin–streptomycin (Cat. no. 15140122; Thermo Fisher Scientific), β-mercaptoethanol (Cat. no. 21985023; Thermo Fisher Scientific), sodium pyruvate (Cat. no. 11360088; Thermo Fisher Scientific), Lipofectamine 3000 (Cat. no.

L3000015; Thermo Fisher Scientific), HBSS (Cat. no. 14025076; Thermo Fisher Scientific), PBS (Cat. no. 10010049; Thermo Fisher Scientific), chloroquine (Cat. no. C6628; Thermo Fisher Scientific), Pierce Protein A/G magnetic beads (Cat. no. 88802; Thermo Fisher Scientific), radioimmunoprecipitation assay (RIPA) lysis and extraction buffer (Cat. no. 89900; Thermo Fisher Scientific), TRIzol reagent (Cat. no. 15596026; Thermo Fisher Scientific), OptiPrep density gradient medium (Cat. no. D1556; Merck), collagenase P (Cat. no. 11249002001; Merck), Pierce BCA Protein Assay Kit (Cat. no. 23227; Thermo Fisher Scientific), EndoFree Mini Plasmid Kit (Cat. no. DP118-02; Tiangen), Mouse Proinsulin ELISA Kit (Cat. no. 80-PINMS-E01; APLCO), Rat/Mouse Insulin ELISA Kit (Cat. no. EZRMI-13K; Merck), Lysosome Isolation Kit (Cat. no. LYSISO1-1KT; Merck), SuperRT cDNA Synthesis Kit (Cat. no. CW0741S; CWBIO), Glutathione Sepharose beads (Cat. no. SA008005; Smart Lifesciences), Ni-NTA agarose beads (Cat. no. 30210; Qiagen).

Mouse models

All animal experiments were performed according to institutional guidelines and approved by the Animal Care Committee of the Institute of Biophysics, Chinese Academy of Sciences. C57BL/6J mice were maintained under a 12-h light–dark cycle in a specific pathogen–free facility at 21–23°C. Healthy mice were monitored through growth curves, random blood glucose tests, and behavioral observations. The details of the mice (age, sex, genotype, and number) used in the study are provided in the appropriate figure legends. VAMP4 KO mice were generated using CRISPR/Cas9-mediated genome engineering by Cyagen Bioscience, Inc. The *Vamp4* gene (GenBank accession number: NM_016796.3) is located on chromosome 1 in the mouse genome. Single-guide RNA (sgRNA) targets were designed by the CRISPR database (http://crispor.tefor.net/), and candidate targets with the strongest score were selected. sgRNA 1 and sgRNA 2 targeted the template and deleted the region of exon 3 to exon 7 by microinjection into mouse zygotes. The sequences (5′–3′) of sgRNA 1 and sgRNA 2 were as follows: 5′-GAAGAGCATTAGGTCCTAAC-3′ (sgRNA 1) and 5′-ATAATGGCATGACTTGACTA-3′ (sgRNA 2). The gene primer sequences (5′–3′) used for identification of the mouse genotype by PCR were as follows: *Vamp4* forward 1, 5′-TCTTGGTTCATACCCTTCCTTCATC-3′; *Vamp4* reverse 1, 5′-GCT GTGTCTTGGGTGTGGCTGAG-3′; and *Vamp4* forward 2, 5′-CAT GTGAGAAGTAGAGAATTGGAC-3′.

Cell lines

The INS-1 rat insulinoma cell line was cultured in RPMI 1640 medium supplemented with 10% FBS, 1% penicillin–streptomycin, 1% sodium pyruvate, and 0.5% β-mercaptoethanol. All cell lines were maintained at 37°C in a 5% CO_2 incubator and tested for mycoplasma contamination. VAMP4 gene-edited cell lines were generated using the CRISPR/Cas9 technique. The rat *Vamp4* gene (GenBank accession number: NM_001108856.1) is located on chromosome 13, and the guide targets were designed by the CRISPR database (http://crispor.tefor.net/). sgRNA was ligated into the pSpCas (BB)-2A-GFP vector and transfected into INS-1 cells. The sequence (5′–3′) of the sgRNA was as follows: 5′-CTAAATGACGATGACGTCAC-3′. GFP-positive cells were sorted and cultured in 96-well plates by FACS. Single clones were selected, expanded, and identified by genotype and Western blot assays. The gene primer sequences (5′–3′) for the PCR assay were as follows: *Vamp4* forward, 5′-GGAGTGGAG CAAGAGTAGGTAGATAAAG-3′, and *Vamp4* reverse, 5′-CCT AAGTTTGGACCCTTGGCATCC-3′.

Mouse islet isolation and culture

Mice were killed by cervical dislocation and perfused with collagenase P at a concentration of 1 mg/ml in the mouse common bile duct (Li et al., 2009). The perfused pancreas was digested in a 37°C water bath for 15 min. After centrifugation, the pellets were washed and suspended in HBSS. Islets were handpicked under a microscope and cultured in RPMI 1640 medium supplemented with 15% FBS and 1% penicillin–streptomycin overnight at 37°C in a 5% CO_2 incubator.

Primary mouse pancreatic β cell isolation and culture

Mouse pancreatic islets were obtained, cultured in RPMI 1640 medium overnight, and then rinsed twice with HBSS. The islets were then dispersed to obtain single cells with 0.05% trypsin for 10 min at 37°C. The dispersed cells were collected by centrifugation at 1,500× *g* for 10 min and resuspended in serum-containing medium supplemented with 10% FBS and 1% penicillin–streptomycin. The dispersed cells were plated onto polylysine-coated coverslips and allowed to settle overnight at 37°C in a 5% CO_2 incubator.

Glucose tolerance test (GTT)

The intraperitoneal GTT has been widely used for assessment of blood glucose levels in vivo. Male mice were fasted overnight and injected with glucose at 2 g/kg body weight. The blood glucose levels in the tail vein were measured at 0, 15, 30, 60, and 120 min using a glucometer.

ITT

The intraperitoneal ITT has been widely used for the assessment of insulin resistance in vivo. Male mice were fasted for 5–6 h and injected with insulin (100 U/ml) at 0.5 U/kg body weight. The circulating blood glucose levels in the tail vein were measured at 0, 15, 30, 60, and 120 min using a glucometer.

Body weight measurements

The body weight was measured every 2 wk starting at 7–17 wk using a laboratory balance to establish the growth curve. Male mice were weighed in the morning at 9 a.m., and the mice found in an unusually nervous or agitated state were not measured. After weighing, each mouse was placed in a new clean cage along with its mates.

Blood biochemical analysis

100 µl of blood were collected in centrifuge tubes without any anticoagulant, and the tubes were maintained in a standing position for 20 min. Subsequently, the blood was clotted and centrifuged at 3,000 rpm at room temperature for 10 min. Serum was collected from clotted blood and transferred to new centrifuge tubes for insulin concentration analysis.

Glucose-stimulated insulin secretion assay

Isolated islets or INS-1 cells were cultured in RPMI 1640 medium in 12-well plates. The culture medium was changed to Krebs-Ringer bicarbonate buffer (KRBB), pH 7.4, containing 129 mM NaCl, 4.7 mM KCl, 1.2 mM KH_2PO_4, 2.5 mM $CaCl_2$, 1.2 mM $MgSO_4$, 5 mM $NaHCO_3$, 10 mM Hepes, and 0.1% BSA. Islets or INS-1 cells were equilibrated for 2 h in KRBB supplemented with 2.8 mM glucose and then incubated for 1 h with KRBB containing either 2.8 or 16.7 mM glucose. The supernatant was collected for analysis of the secreted insulin levels using an insulin ELISA kit following the manufacturer's instructions. The islets or cells were collected by centrifugation at 1,500 rpm for 10 min. The level of insulin secretion from isolated pancreatic islets was normalized to the cell number, and the level of insulin secretion from INS-1 cells was normalized to the intracellular protein content.

Immunohistochemistry analysis

Immunohistochemistry was performed according to a standard protocol. Pancreases were isolated from the mice, fixed in 4% PFA for 48–72 h at 4°C, and then transferred to 70% ethanol. The pancreases were embedded in paraffin, and 5-µm slices were obtained at 200-µm intervals from each pancreas. For the morphological analysis of mouse islets, five slices from each mouse were used for hematoxylin and eosin (H&E) staining and scanned with a Leica CS2 system.

Immunofluorescence analysis

For immunofluorescence assay, pancreatic slices and cell samples were fixed in 4% PFA for 15 min, permeabilized with 0.1% Triton X-100 for 10 min, and blocked with 5% BSA for 1 h at room temperature. The samples were then incubated with 3% BSA containing primary antibodies overnight at 4°C (anti-VAMP4 at 1:100 dilution, anti-insulin at 1:400 dilution, anti-glucagon at 1:100 dilution, and anti-proinsulin at 1:100 dilution). The next day, the samples were washed six times for 5 min each and incubated with Alexa Fluor–labeled secondary antibody (1:200) containing 3% BSA for 1 h at room temperature. After washing, the samples were dried and coverslipped with mounting medium containing DAPI. All solutions and reagents were diluted in PBS at pH 7.4.

Construction of plasmids

The DNA fragments encoding mCherry and Halo were generated by PCR and cloned into the AgeI-XbaI restriction sites of the pEGFP-N1 vector. The DNA fragments of EYFP encoding the N-terminal 1–154 amino acid residues (nYFP) and C-terminal 155–239 amino acid residues (cYFP) were generated by PCR and cloned into the NheI-SacI restriction sites of the pEGFP-C1 vector (Hu et al., 2002; Tsugama et al., 2012). The DNA fragments encoding VAMP4, STX7, STX8, and VTI1B were generated by PCR and fused to the nYFP and cYFP vectors via the restriction sites EcoRI-BamHI. The DNA fragments encoding VAMP4 were generated by PCR and cloned into the EcoRI-BamHI restriction sites of the pEGFP-C1 vector. The DNA fragments encoding LAMP1 were generated by PCR and cloned into the KpnI-BamHI restriction sites of the pmCherry-N1 and pHalo-N1 vectors. The DNA fragments encoding clathrin were generated by PCR and cloned into the KpnI-Age1 restriction sites of the pmCherry-N1 vector. The DNA fragments of proinsulin encoding the N-terminal 1–59 (B-C peptide) and C-terminal 60–110 amino acid residues (C-A peptide) were generated by PCR, fused with mCherry and Halo sequences between the B-C and C-A peptides and cloned into the XmaI-NotI restriction sites of the pEGFP-N1 vector. The following primer sequences (5′–3′) were used for plasmid construction: mCherry forward, 5′-CCACCGGTCGCCACCATGGTGAGCAAGGGCGAGGA-3′, and mCherry reverse, 3′-TCTAGAGTCGCGGCCGCTACTTGTACAGCTCGTCCAT-5′; Halo forward, 5′-CTAGCTAGCGCTACCGGTCGCCACCATGGCAGAAATCGGTACTGGC-3′, and Halo reverse, 3′-CCGGAATTCGAAGCTTGAGCTCGAGATCTGAGTCCGGAGCCGGAAATCTCGAGCGTC-5′; nYFP forward, 5′-GCTAGCACCGGTCGCCACCATGGTGAGCAAGGGCGAG-3′, and nYFP reverse, 3′-CTCGAGCTGTGGCTATGCTCCTGGCCATGATATAGACGTTGTGGC-5′; cYFP forward, 5′-GCTAGCACCGGTCGCCACCATGGACAAGCAGAAGAACGGCATC-3′, and cYFP reverse, 3′-CTCGAGCTGTGGCTATGCTCCTCTTGTACAGCTCGTCCATGC-5′; STX7 forward, 5′-GAATTCTGCAGTCGACATGTCTTACACTCCAGGAGTTGGT-3′, and STX7 reverse, 3′-GGATCCTCAGTGGTTCAATCCCCATATGATGAGA-5′; STX8 forward, 5′-GAATTCTGCAGTCGACATGGCACCGGACCCC-3′, and STX8 reverse, 3′GGATCCTCAGTTGGTCGGCCAGACTG-5′; VTI1B forward, 5′-GAATTCTGCAGTCGACATGGCCTCCTCCGCC-3′, and VTI1B reverse, 3′-GGATCCTCAATGGCTGCGAAAGAATTTGTAGT-5′; VAMP4 forward, 5′-TCGAATTCTGCAGTCGACATGCCTCCCAAGTTTAAGCGC-3′, and VAMP4 reverse, 3′-GCGGGATCCTCAAGTACGGTATTTCATGACT-5′; LAMP1 forward, 5′-AATTCTCGCCACCATGGCGGCCCCGGGCGCCCGGCGGCCGCTGCTC-3′, and LAMP1 reverse, 3′-GCGGGATCCCGGATGGTCTGATAGCCCG-5′; clathrin forward, 5′-ACGGTACCATGGCCGAGTTGGATCC-3′, and clathrin reverse, 3′-GGCGACCGGTTTCAGTGCACCAG-5′; and insulin forward, 5′-CCCGGGATCCGCCACCATGGCCCTGTGGATGCG-3′, and insulin reverse, 3′-GTCGCGGCCGCTCAGTTGCAGTAGTTCTCCAGTTGGT-5′.

Fixed-sample fluorescence imaging

Images of the samples were captured at room temperature using an FV 1200 laser scanning confocal microscope (Olympus). Images of the pancreatic sections were obtained with a 40× (NA = 1.30) oil objective, and cell sample images were acquired with a 60× (NA = 1.40) oil objective. ImageJ was used to analyze the fluorescence intensity, the area of the islets, and the cell numbers.

Live-cell fluorescence imaging

Deconvolution microscopy

INS-1 cells were cultured on glass-bottom dishes for 24 h and then transfected with 2 µg of plasmids containing mCherry-tagged LAMP1, Halo-tagged LAMP1, mCherry-tagged (pro)insulin, mCherry-tagged clathrin, or EGFP-tagged VAMP4 using Lipofectamine 3000. 48 h later, long-term live-cell imaging was performed in RPMI 1640 medium at 37°C in an atmosphere with 5% CO_2 using a Delta Vision OMX V3 system (GE Healthcare) with a 100× (NA = 1.40) oil objective. Fluorescence images were collected in the wide-field mode with an exposure time of 0.01 s

and a 0.5-s interval between frames or no time-lapse for one stack. The deconvolution images were analyzed and aligned using softWoRx software (GE Healthcare). Vesicle tracking and detection were performed using Imaris software (version 9.5, Bitplane) according to the time points.

Super-resolution confocal microscopy

Live-cell imaging was performed using a Zeiss LSM 980 with Airyscan (Carl Zeiss). 48 h after transfection of a plasmid combination of nYFP-tagged VAMP4 with nYFP-tagged STX7, cYFP-tagged STX7, nYFP-tagged STX8, cYFP-tagged STX8, nYFP-tagged VTI1B, or cYFP-tagged VTI1B, cells were imaged in RPMI 1640 medium at 37°C in an atmosphere with 5% CO_2 using an 100× (NA = 1.40) objective and immersion oil optimized for 30°C (Carl Zeiss). Airyscan processing was performed using the Airyscan module in ZEN software (Carl Zeiss).

Western blot analysis

Isolated islets or cell pellets were suspended in strong RIPA buffer (150 mM NaCl, 1% NP-40, 0.5% deoxycholic acid, 0.1% SDS, and 50 mM Trizma base, pH 8.0) containing protease inhibitor on ice for 30 min. Cell lysates were centrifuged at 15,000 rpm at 4°C for 15 min, and postnuclear supernatant (PNS) was collected. The protein concentration was determined using a BCA protein assay. Protein was adjusted to 20 mg per sample and separated by 12% SDS–PAGE based on the molecular weight. The protein sample was transferred to a 0.45-µm polyvinylidine fluoride membrane and blocked with 5% nonfat milk in TBST buffer (150 mM NaCl, 0.1% Triton X-100, and 25 mM Trizma base, pH 7.6) for 1 h at room temperature. The membrane was incubated with primary antibody overnight at 4°C, rinsed six times for 5 min each, and probed with HRP-conjugated secondary antibody (anti-mouse, anti-rabbit, or anti-pig) for 1 h at room temperature. Most primary antibodies were diluted 1:1,000, and the secondary antibodies were diluted 1:5,000. The target protein signals were detected by enhanced chemiluminescence using an imaging system (ChemiScope 6100 Touch, ClinX). The acquired images were further processed with Adobe Photoshop CS6 and analyzed using ImageJ.

Insulin granule enrichment

INS-1 cells were grown on 10-cm diameter dishes, harvested by trypsin, and centrifuged at 1,500 rpm at 4°C for 10 min. Cell pellets were suspended in 2 ml homogenization buffer (0.3 M sucrose, 1 mM EDTA, 1 mM $MgSO_4$, 10 mM MES-KOH, pH 6.5) supplemented with protease inhibitor by nitrogen cavitation for 15 min at 500 psi on ice. Cell lysates were centrifuged at 5,000 rpm at 4°C for 15 min, and PNS was collected and loaded on top of a discontinuous Optiprep gradient composed of five layers (8.8, 13.2, 17.6, 23.4, 30%). The samples were centrifuged at 10,000× *g* at 4°C for 135 min in an SW40 tube. The enrichment fractions were collected and suspended in strong RIPA buffer, and equal volumes of the fractions were loaded on 10% NuPAGE gels for Western blot assays.

Lysosome enrichment

Lysosome enrichment was performed using a lysosome isolation kit according to the manufacturer's recommended protocol. Fresh cell pellets were suspended in 1× extraction buffer containing protease inhibitor and homogenized in a Dounce homogenizer. Cell lysate was centrifuged at 1,500× *g* at 4°C for 15 min to remove nuclei. The PNS was centrifuged at 20,000× *g* at 4°C for 20 min to obtain the crude lysosomal fraction.

Immunoprecipitation assay

The lysosomal fraction was suspended in 1× extraction buffer containing 8 mM $CaCl_2$ on ice for 20 min and then sonicated for 3 min. The cell lysate or lysosomal fraction was centrifuged at 15,000 rpm at 4°C for 15 min. The supernatant was collected in a tube and incubated with primary antibody overnight at 4°C with gentle rotation, and 100 µl of supernatant was saved as input. The next day, prewashed protein A/G magnetic beads were added to the tube for 1 h at 4°C. The magnetic beads were washed five times with wash buffer (150 mM NaCl, 1 mM EDTA, 25 mM Trizma base, pH 7.4). The beads were boiled with 1× SDS loading buffer at 95°C for 10 min and analyzed by Western blot assay.

Protein expression and purification

The plasmids pET.MBP.3C.hVTI1B (1–204), pET.MEKTR.3C.hSTX7 (1–236), pET.32 M.3C.hSTX8 (1–210), pGEX-6P-1.hVAMP4 (1–115), and pGEX-6P-1 were a gift from Dr. Hong Zhang. The recombinant protein was expressed in Transetta(DE3) chemically competent cells and cultured in LB (1% yeast extract, 1% tryptone, and 0.5% NaCl) medium at 37°C to OD_{600} ≈ 1.0. To induce protein expression, 1 mM IPTG was added, and the cells were continuously cultured overnight at 18 or 25°C with shaking at 200 rpm. The *Escherichia coli* cells were collected by centrifugation at 4,000 rpm for 20 min. For protein purification, the collected cells were suspended in binding buffer (140 mM NaCl, 2.7 mM KCl, 10 mM Na_2HPO_4, and 1.8 mM KH_2PO_4, pH 7.4) containing a protease inhibitor cocktail and lysed bacterial spores by sonication and centrifuged at 10,000 rpm at 4°C for 30 min. The lysate (His-tagged STX7, STX8, and VTI1B) supernatants were affinity purified with Ni-NTA agarose beads, and the lysate (GST and GST-tagged VAMP4) supernatants were affinity purified with Glutathione Sepharose beads. The lysate and beads were incubated with gentle rotation for 1 h at 4°C and then washed with binding buffer. His-tagged bound proteins were eluted with binding buffer containing 200 mM imidazole, and GST-tagged bound proteins were eluted with binding buffer containing 10 mM reduced glutathione and 1 mM DTT. The purified SNARE proteins (VAMP4-STX7-STX8-VTI1B/GST-STX7-STX8-VTI1B) at molar mass ratio of 1:1:1:1 were incubated with a protease inhibitor cocktail overnight at 4°C. The complex was conjugated to GST beads, washed extensively, and eluted with binding buffer containing 10 mM reduced glutathione and 1 mM DTT. The bound proteins were boiled in 5× SDS sample loading buffer at 95°C for 10 min and analyzed by SDS–PAGE and Coomassie blue staining.

Cell transfection and siRNA

We used two specific siRNA sequences to knock down STX7 and STX8 and thus decrease the levels of these proteins. The cells were cultured in 6-well plates and transfected with 100 nM

scramble RNA as a negative control or with a mixture of two siRNA alleles targeting STX7 and STX8 using Lipofectamine 3000 transfection reagent. 72 h after transfection, the cell plate and supernatant for glucose stimulation were collected and detected by Western blot and ELISAs. The siRNA sequences were as follows: siCtrl, 5′-UUCUCCAACGUGUCAGUT-3′; siSTX7 1, 5′-GCGAAAGAAACAGAUAAGUTT-3′; siSTX7 2, 5′-GCGCUAACAAACUUUCAGATT-3′; siSTX8 1, 5′-CUACUUGUCAGAUUGCCCATT-3′; and siSTX8 2, 5′-CUCCUGGCAUCGUUUAAGATT-3′.

Transmission EM

Mouse pancreatic islets were isolated from 16-wk-old male mice and fixed in 2.5% glutaraldehyde in PBS at pH 7.4 for 24 h at 4°C. The samples were postfixed in 1% osmium tetroxide in 0.1 M sodium cacodylate for 1 h and then in 1% (wt/vol) uranyl acetate for 30 min and embedded in Spurr's resin after dehydration in a graded series of acetone (Xue et al., 2012). Ultrathin sections (60 nm) were cut using a diamond knife and picked up on 1% pioloform-coated copper slot grids for observation by transmission EM. Images of whole-cell sections were captured at 100 kV and a magnification of 4,800×. Additionally, images of the regions of interest were captured at 120 kV and a magnification of 23,000×. Quantification of the ISGs and ISG-lysosome interactions per β cell was performed using serial EM software to obtain an automated montage overview of a map at a magnification of 18,500×, and the results were normalized to the area of the cytoplasm using ImageJ software (Schorb et al., 2019).

Quantitative RT–PCR assay

For RT–PCR analysis, total RNA from INS-1 cells was extracted using TRIzol reagent according to a standard protocol. The RNA quality was assessed by agarose gel electrophoresis, and the A260/A280 and A260/A230 ratios were measured. Reverse transcription to obtain cDNA was performed with 2 μg of total RNA using a SuperRT cDNA Synthesis Kit. RT-PCRs were performed on a QuantStudio 7 using specific primers and SYBR Green master mix. The change in gene expression was calculated using the $2^{-\Delta\Delta Ct}$ method with normalization to the expression of *18S*. The sequences (5'–3') of the primers used for RT–PCR experiments were as follows: *Ins* forward, 5′-CAGTTGGTAGAGGGAGCAGAT-3′, and *Ins* reverse, 3′-CCGTCGTGAAGTGGAGGA-5′; *18S* forward, 5′-GTAACCCGTTGAACCCCATT-3′, and *18S* reverse, 3′-CCATCCAATCGGTAGTAGCG-5′; *Pc1* forward, 5′-AGTAAAGCAACCCAGAGCCAG-3′, and *Pc1* reverse, 3′-AGTGCACACCAAACGCAAAA-5′; and *Pc2* forward, 5′-CAGGTATCCGGATGCTGGAC-3′, and *Pc2* reverse, 3′-TCTTCCTCCCGTTGCTGAAC-5′.

Statistical analysis

The biological samples, technical replicates per sample, and P values are appropriately described in the figure legends. For all in vivo mouse studies, the mice were randomly assigned to groups, and the *n* value corresponds to the individual mouse results. For live-cell imaging, a Gaussian filter was used to smoothly display the images and reduce noise with Imaris software. The statistical significance of the differences between two groups was determined using two-tailed unpaired Student's *t* tests, as the sample groups displayed a normal distribution and comparable variance assessment by SPSS software (IBM SPSS statistics 26). One-way ANOVA with repeated measures was used to analyze the data from Western blotting, proinsulin/insulin ELISA analysis, and RT–PCR, and two-way ANOVA was used to analyze the ISG percentage and lysosome inhibitor data. All values in the graphs are represented as the mean ± SEM using GraphPad Prism Software 7 and Microsoft Excel analysis. A P value <0.05 was considered to indicate significance and is indicated by an asterisk (*, $P < 0.05$; **, $P < 0.01$; ***, $P < 0.001$; ****, $P < 0.0001$).

Online supplemental material

Fig. S1 shows that VAMP4 KO mice exhibit hyperresponsiveness to glucose. Fig. S2 shows that VAMP4 deficiency causes increases in intracellular (pro)insulin and insulin release. Fig. S3 shows that VAMP4 is packaged into clathrin-coated iISGs near the TGNs and VAMP4-positive vesicles fuse with lysosomes. Fig. S4 shows that VAMP4 facilitates the fusion of iISGs and resorted vesicles with lysosomes for granule cargo degradation. Fig. S5 shows that VAMP4 regulates the insulin levels by facilitating the membrane fusion of iISGs and resorted vesicles with lysosomes. Video 1 shows the intracellular trafficking of VAMP4-positive vesicles and insulin granules in vivo. Video 2 shows the intracellular trafficking of VAMP4-positive vesicles and lysosomes in vivo. Video 3 shows the intracellular trafficking of insulin granules and lysosomes in vivo.

Data availability

The authors declare that all data and materials supporting the findings of this study are available and that requests for materials should be addressed to Eli Song or Tao Xu.

Acknowledgments

We thank the Center of Biological Imaging at the Institute of Biophysics, Chinese Academy of Sciences, for the confocal microscopy, EM, and SIM imaging. We are grateful to Dr. Yan Teng and her group for helping with the confocal imaging, Dr. Shuoguo Li for the technical support provided with the live-cell imaging using the Delta Vision OMX V3 system, Dr. Yun Feng for the assistance with the imaging data analysis, Dr. Junying Jia and Dr. Shu Meng for the technical support with the flow cytometry analysis, and Dr. Hong Zhang and Dr. Zheng Wang (Institute of Biophysics, Chinese Academy of Sciences, Beijing, China) for the gift of plasmids for protein expression.

This work was supported by grants from the Ministry of Science and Technology of the People's Republic of China (2021YFA1300301, 2018YFA0507101), the National Natural Science Foundation of China (31730054, 31770900), and the Beijing Natural Science Foundation (5212016).

The authors declare no competing financial interests.

Author contributions: M. Li performed most of the experiments and data analyses and wrote the manuscript. F. Feng performed the EM experiments. H. Feng helped with the experimental design and data analyses. P. Hu helped with the biochemical experiments. Y. Xue helped with the EM analyses.

E. Song and T. Xu conceptualized the study, supervised the experiments, acquired funding, and wrote the paper.

Submitted: 29 October 2021
Revised: 28 June 2022
Accepted: 25 July 2022

References

Advani, R.J., H.R. Bae, J.B. Bock, D.S. Chao, Y.C. Doung, R. Prekeris, J.S. Yoo, and R.H. Scheller. 1998. Seven novel mammalian SNARE proteins localize to distinct membrane compartments. *J. Biol. Chem.* 273: 10317–10324. https://doi.org/10.1074/jbc.273.17.10317

Arvan, P., and D. Castle. 1998. Sorting and storage during secretory granule biogenesis: Looking backward and looking forward. *Biochem. J.* 332: 593–610. https://doi.org/10.1042/bj3320593

Bonnemaison, M.L., B.A. Eipper, and R.E. Mains. 2013. Role of adaptor proteins in secretory granule biogenesis and maturation. *Front. Endocrinol.* 4:101. https://doi.org/10.3389/fendo.2013.00101

Bostrom, P., L. Andersson, M. Rutberg, J. Perman, U. Lidberg, B.R. Johansson, J. Fernandez-Rodriguez, J. Ericson, T. Nilsson, J. Boren, and S.O. Olofsson. 2007. SNARE proteins mediate fusion between cytosolic lipid droplets and are implicated in insulin sensitivity. *Nat. Cell Biol.* 9: 1286–1293. https://doi.org/10.1038/ncb1648

Brandhorst, D., D. Zwilling, S.O. Rizzoli, U. Lippert, T. Lang, and R. Jahn. 2006. Homotypic fusion of early endosomes: SNAREs do not determine fusion specificity. *Proc. Natl. Acad. Sci. USA.* 103:2701–2706. https://doi.org/10.1073/pnas.0511138103

Campbell, J.E., and C.B. Newgard. 2021. Mechanisms controlling pancreatic islet cell function in insulin secretion. *Nat. Rev. Mol. Cell Biol.* 22: 142–158. https://doi.org/10.1038/s41580-020-00317-7

Chen, Y.A., and R.H. Scheller. 2001. SNARE-mediated membrane fusion. *Nat. Rev. Mol. Cell Biol.* 2:98–106. https://doi.org/10.1038/35052017

Cheng, D., L. Zheng, J. Hou, J. Wang, P. Xue, F. Yang, and T. Xu. 2015. A new dimethyl labeling-based SID-MRM-MS method and its application to three proteases involved in insulin maturation. *Biophys. Rep.* 1:71–80. https://doi.org/10.1007/s41048-015-0012-1

Csizmadia, T., and G. Juhasz. 2020. Crinophagy mechanisms and its potential role in human health and disease. *Prog. Mol. Biol. Transl. Sci.* 172: 239–255. https://doi.org/10.1016/bs.pmbts.2020.02.002

Csizmadia, T., P. Lorincz, K. Hegedus, S. Szeplaki, P. Low, and G. Juhasz. 2018. Molecular mechanisms of developmentally programmed crinophagy in *Drosophila*. *J. Cell Biol.* 217:361–374. https://doi.org/10.1083/jcb.201702145

Davidson, H.W. 2004. (Pro)Insulin processing: A historical perspective. *Cell Biochem. Biophys.* 40:143–158. https://doi.org/10.1385/cbb:40:3:143

Dingjan, I., P.T.A. Linders, D.R.J. Verboogen, N.H. Revelo, M. Ter Beest, and G. van den Bogaart. 2018. Endosomal and phagosomal SNAREs. *Physiol. Rev.* 98:1465–1492. https://doi.org/10.1152/physrev.00037.2017

Du, W., M. Zhou, W. Zhao, D. Cheng, L. Wang, J. Lu, E. Song, W. Feng, Y. Xue, P. Xu, and T. Xu. 2016. HID-1 is required for homotypic fusion of immature secretory granules during maturation. *Elife.* 5:e18134. https://doi.org/10.7554/eLife.18134

Eaton, B.A., M. Haugwitz, D. Lau, and H.P. Moore. 2000. Biogenesis of regulated exocytotic carriers in neuroendocrine cells. *J. Neurosci.* 20: 7334–7344. https://doi.org/10.1523/jneurosci.20-19-07334.2000

Eliasson, L., F. Abdulkader, M. Braun, J. Galvanovskis, M.B. Hoppa, and P. Rorsman. 2008. Novel aspects of the molecular mechanisms controlling insulin secretion. *J. Physiol.* 586:3313–3324. https://doi.org/10.1113/jphysiol.2008.155317

Feldmann, A., C. Winterstein, R. White, J. Trotter, and E.M. Kramer-Albers. 2009. Comprehensive analysis of expression, subcellular localization, and cognate pairing of SNARE proteins in oligodendrocytes. *J. Neurosci. Res.* 87:1760–1772. https://doi.org/10.1002/jnr.22020

Furuta, N., N. Fujita, T. Noda, T. Yoshimori, and A. Amano. 2010. Combinational soluble *N*-ethylmaleimide-sensitive factor attachment protein receptor proteins VAMP8 and Vti1b mediate fusion of antimicrobial and canonical autophagosomes with lysosomes. *Mol. Biol. Cell.* 21:1001–1010. https://doi.org/10.1091/mbc.e09-08-0693

Goginashvili, A., Z. Zhang, E. Erbs, C. Spiegelhalter, P. Kessler, M. Mihlan, A. Pasquier, K. Krupina, N. Schieber, L. Cinque, et al. 2015. Insulin granules. Insulin secretory granules control autophagy in pancreatic β cells. *Science.* 347:878–882. https://doi.org/10.1126/science.aaa2628

Halban, P.A. 1991. Structural domains and molecular lifestyles of insulin and its precursors in the pancreatic β cell. *Diabetologia.* 34:767–778. https://doi.org/10.1007/BF00408349

Halban, P.A., and C.B. Wollheim. 1980. Intracellular degradation of insulin stores by rat pancreatic islets in vitro. An alternative pathway for homeostasis of pancreatic insulin content. *J. Biol. Chem.* 255:6003–6006. https://doi.org/10.1016/s0021-9258(18)43686-1

Hinke, S.A., K. Hellemans, and F.C. Schuit. 2004. Plasticity of the β cell insulin secretory competence: Preparing the pancreatic β cell for the next meal. *J. Physiol.* 558:369–380. https://doi.org/10.1113/jphysiol.2004.064881

Hirata, T., M. Fujita, S. Nakamura, K. Gotoh, D. Motooka, Y. Murakami, Y. Maeda, and T. Kinoshita. 2015. Post-Golgi anterograde transport requires GARP-dependent endosome-to-TGN retrograde transport. *Mol. Biol. Cell.* 26:3071–3084. https://doi.org/10.1091/mbc.E14-11-1568

Hou, J.C., L. Min, and J.E. Pessin. 2009. Insulin granule biogenesis, trafficking and exocytosis. *Vitam. Horm.* 80:473–506. https://doi.org/10.1016/S0083-6729(08)00616-X

Howell, S.L., and G.S. Bird. 1989. Biosynthesis and secretion of insulin. *Br. Med. Bull.* 45:19–36. https://doi.org/10.1093/oxfordjournals.bmb.a072311

Hu, C.D., Y. Chinenov, and T.K. Kerppola. 2002. Visualization of interactions among bZIP and Rel family proteins in living cells using bimolecular fluorescence complementation. *Mol. Cell.* 9:789–798. https://doi.org/10.1016/s1097-2765(02)00496-3

Ivanova, D., K.L. Dobson, A. Gajbhiye, E.C. Davenport, D. Hacker, S.K. Ultanir, M. Trost, and M.A. Cousin. 2021. Control of synaptic vesicle release probability via VAMP4 targeting to endolysosomes. *Sci. Adv.* 7:eabf3873. https://doi.org/10.1126/sciadv.abf3873

Jena, B.P. 2011. Role of SNAREs in membrane fusion. *Adv. Exp. Med. Biol.* 713: 13–32. https://doi.org/10.1007/978-94-007-0763-4_3

Kreykenbohm, V., D. Wenzel, W. Antonin, V. Atlachkine, and G.F. von Mollard. 2002. The SNAREs vti1a and vti1b have distinct localization and SNARE complex partners. *Eur. J. Cell Biol.* 81:273–280. https://doi.org/10.1078/0171-9335-00247

Lawrence, R.E., and R. Zoncu. 2019. The lysosome as a cellular centre for signalling, metabolism and quality control. *Nat. Cell Biol.* 21:133–142. https://doi.org/10.1038/s41556-018-0244-7

Lee, Y.H., J. Kim, K. Park, and M.S. Lee. 2019. β-cell autophagy: Mechanism and role in β-cell dysfunction. *Mol. Metabol.* 27S:S92–S103. https://doi.org/10.1016/j.molmet.2019.06.014

Li, D.S., Y.H. Yuan, H.J. Tu, Q.L. Liang, and L.J. Dai. 2009. A protocol for islet isolation from mouse pancreas. *Nat. Protoc.* 4:1649–1652. https://doi.org/10.1038/nprot.2009.150

Li, M., W. Du, M. Zhou, L. Zheng, E. Song, and J. Hou. 2018. Proteomic analysis of insulin secretory granules in INS-1 cells by protein correlation profiling. *Biophys. Rep.* 4:329–338. https://doi.org/10.1007/s41048-018-0061-3

Littleton, J.T., T.L. Serano, G.M. Rubin, B. Ganetzky, and E.R. Chapman. 1999. Synaptic function modulated by changes in the ratio of synaptotagmin I and IV. *Nature.* 400:757–760. https://doi.org/10.1038/23462

Luzio, J.P., P.R. Pryor, and N.A. Bright. 2007. Lysosomes: Fusion and function. *Nat. Rev. Mol. Cell Biol.* 8:622–632. https://doi.org/10.1038/nrm2217

Malide, D., N.G. Seidah, M. Chretien, and M. Bendayan. 1995. Electron microscopic immunocytochemical evidence for the involvement of the convertases PC1 and PC2 in the processing of proinsulin in pancreatic β-cells. *Journal Histochem. Cytochem.* 43:11–19. https://doi.org/10.1177/43.1.7822759

Mallard, F., B.L. Tang, T. Galli, D. Tenza, A. Saint-Pol, X. Yue, C. Antony, W. Hong, B. Goud, and L. Johannes. 2002. Early/recycling endosomes-to-TGN transport involves two SNARE complexes and a Rab6 isoform. *J. Cell Biol.* 156:653–664. https://doi.org/10.1083/jcb.200110081

Marsh, B.J., C. Soden, C. Alarcon, B.L. Wicksteed, K. Yaekura, A.J. Costin, G.P. Morgan, and C.J. Rhodes. 2007. Regulated autophagy controls hormone content in secretory-deficient pancreatic endocrine β-cells. *Mol. Endocrinol.* 21:2255–2269. https://doi.org/10.1210/me.2007-0077

Martin, S.K., R. Carroll, M. Benig, and D.F. Steiner. 1994. Regulation by glucose of the biosynthesis of PC2, PC3 and proinsulin in (ob/ob) mouse islets of Langerhans. *FEBS Lett.* 356:279–282. https://doi.org/10.1016/0014-5793(94)01284-9

Mauthe, M., I. Orhon, C. Rocchi, X. Zhou, M. Luhr, K.J. Hijlkema, R.P. Coppes, N. Engedal, M. Mari, and F. Reggiori. 2018. Chloroquine inhibits autophagic flux by decreasing autophagosome-lysosome fusion. *Autophagy.* 14:1435–1455. https://doi.org/10.1080/15548627.2018.1474314

McNew, J.A., F. Parlati, R. Fukuda, R.J. Johnston, K. Paz, F. Paumet, T.H. Sollner, and J.E. Rothman. 2000. Compartmental specificity of cellular

membrane fusion encoded in SNARE proteins. *Nature*. 407:153–159. https://doi.org/10.1038/35025000

Naggert, J.K., L.D. Fricker, O. Varlamov, P.M. Nishina, Y. Rouille, D.F. Steiner, R.J. Carroll, B.J. Paigen, and E.H. Leiter. 1995. Hyperproinsulinaemia in obese fat/fat mice associated with a carboxypeptidase E mutation which reduces enzyme activity. *Nat. Genet.* 10:135–142. https://doi.org/10.1038/ng0695-135

Orci, L., M. Ravazzola, M. Amherdt, O. Madsen, A. Perrelet, J.D. Vassalli, and R.G. Anderson. 1986. Conversion of proinsulin to insulin occurs coordinately with acidification of maturing secretory vesicles. *J. Cell Biol.* 103:2273–2281. https://doi.org/10.1083/jcb.103.6.2273

Orci, L., M. Ravazzola, M. Amherdt, C. Yanaihara, N. Yanaihara, P. Halban, A.E. Renold, and A. Perrelet. 1984. Insulin, not C-peptide (proinsulin), is present in crinophagic bodies of the pancreatic B-cell. *J. Cell Biol.* 98: 222–228. https://doi.org/10.1083/jcb.98.1.222

Pasquier, A., K. Vivot, E. Erbs, C. Spiegelhalter, Z. Zhang, V. Aubert, Z. Liu, M. Senkara, E. Maillard, M. Pinget, et al. 2019. Lysosomal degradation of newly formed insulin granules contributes to β cell failure in diabetes. *Nat. Commun.* 10:3312. https://doi.org/10.1038/s41467-019-11170-4

Prekeris, R., B. Yang, V. Oorschot, J. Klumperman, and R.H. Scheller. 1999. Differential roles of syntaxin 7 and syntaxin 8 in endosomal trafficking. *Mol. Biol. Cell*. 10:3891–3908. https://doi.org/10.1091/mbc.10.11.3891

Pryor, P.R., B.M. Mullock, N.A. Bright, M.R. Lindsay, S.R. Gray, S.C.W. Richardson, A. Stewart, D.E. James, R.C. Piper, and J.P. Luzio. 2004. Combinatorial SNARE complexes with VAMP7 or VAMP8 define different late endocytic fusion events. *EMBO Rep.* 5:590–595. https://doi.org/10.1038/sj.embor.7400150

Regazzi, R., M. Ravazzola, M. Iezzi, J. Lang, A. Zahraoui, E. Andereggen, P. Morel, Y. Takai, and C.B. Wollheim. 1996a. Expression, localization and functional role of small GTPases of the Rab3 family in insulin-secreting cells. *J. Cell Sci.* 109:2265–2273. https://doi.org/10.1242/jcs.109.9.2265

Regazzi, R., K. Sadoul, P. Meda, R.B. Kelly, P.A. Halban, and C.B. Wollheim. 1996b. Mutational analysis of VAMP domains implicated in Ca^{2+}-induced insulin exocytosis. *EMBO J.* 15:6951–6959. https://doi.org/10.1002/j.1460-2075.1996.tb01087.x

Riahi, Y., J.D. Wikstrom, E. Bachar-Wikstrom, N. Polin, H. Zucker, M.S. Lee, W. Quan, L. Haataja, M. Liu, P. Arvan, et al. 2016. Autophagy is a major regulator of β cell insulin homeostasis. *Diabetologia*. 59:1480–1491. https://doi.org/10.1007/s00125-016-3868-9

Rizzoli, S.O., I. Bethani, D. Zwilling, D. Wenzel, T.J. Siddiqui, D. Brandhorst, and R. Jahn. 2006. Evidence for early endosome-like fusion of recently endocytosed synaptic vesicles. *Traffic*. 7:1163–1176. https://doi.org/10.1111/j.1600-0854.2006.00466.x

Roder, P.V., B. Wu, Y. Liu, and W. Han. 2016. Pancreatic regulation of glucose homeostasis. *Exp. Mol. Med.* 48:e219. https://doi.org/10.1038/emm.2016.6

Rorsman, P., and M. Braun. 2013. Regulation of insulin secretion in human pancreatic islets. *Annu. Rev. Physiol.* 75:155–179. https://doi.org/10.1146/annurev-physiol-030212-183754

Rorsman, P., and E. Renstrom. 2003. Insulin granule dynamics in pancreatic β cells. *Diabetologia*. 46:1029–1045. https://doi.org/10.1007/s00125-003-1153-1

Schnell, A.H., I. Swenne, and L.A. Borg. 1988. Lysosomes and pancreatic islet function. A quantitative estimation of crinophagy in the mouse pancreatic B-cell. *Cell Tissue Res.* 252:9–15. https://doi.org/10.1007/BF00213820

Schorb, M., I. Haberbosch, W.J.H. Hagen, Y. Schwab, and D.N. Mastronarde. 2019. Software tools for automated transmission electron microscopy. *Nat. Methods*. 16:471–477. https://doi.org/10.1038/s41592-019-0396-9

Smith, R.E., and M.G. Farquhar. 1966. Lysosome function in the regulation of the secretory process in cells of the anterior pituitary gland. *J. Cell Biol.* 31:319–347. https://doi.org/10.1083/jcb.31.2.319

Steegmaier, M., J. Klumperman, D.L. Foletti, J.S. Yoo, and R.H. Scheller. 1999. Vesicle-associated membrane protein 4 is implicated in trans-Golgi network vesicle trafficking. *Mol. Biol. Cell*. 10:1957–1972. https://doi.org/10.1091/mbc.10.6.1957

Steiner, D.F., S.Y. Park, J. Stoy, L.H. Philipson, and G.I. Bell. 2009. A brief perspective on insulin production. *Diabetes Obesity Metabol.* 11:189–196. https://doi.org/10.1111/j.1463-1326.2009.01106.x

Suckale, J., and M. Solimena. 2010. The insulin secretory granule as a signaling hub. *Trends Endocrinol. Metabol.* 21:599–609. https://doi.org/10.1016/j.tem.2010.06.003

Tran, T.H.T., Q. Zeng, and W. Hong. 2007. VAMP4 cycles from the cell surface to the trans-Golgi network via sorting and recycling endosomes. *J. Cell Sci.* 120:1028–1041. https://doi.org/10.1242/jcs.03387

Tsugama, D., H. Liu, S. Liu, and T. Takano. 2012. Arabidopsis heterotrimeric G protein β subunit interacts with a plasma membrane 2C-type protein phosphatase, PP2C52. *Biochim. Biophys. Acta*. 1823:2254–2260. https://doi.org/10.1016/j.bbamcr.2012.10.001

Turner, M.D., and P. Arvan. 2000. Protein traffic from the secretory pathway to the endosomal system in pancreatic β-cells. *J. Biol. Chem.* 275: 14025–14030. https://doi.org/10.1074/jbc.275.19.14025

Uchizono, Y., C. Alarcon, B.L. Wicksteed, B.J. Marsh, and C.J. Rhodes. 2007. The balance between proinsulin biosynthesis and insulin secretion: Where can imbalance lead? *Diabetes Obesity Metabol.* 9:56–66. https://doi.org/10.1111/j.1463-1326.2007.00774.x

Vakilian, M., Y. Tahamtani, and K. Ghaedi. 2019. A review on insulin trafficking and exocytosis. *Gene*. 706:52–61. https://doi.org/10.1016/j.gene.2019.04.063

Wang, T., L. Li, and W. Hong. 2017. SNARE proteins in membrane trafficking. *Traffic*. 18:767–775. https://doi.org/10.1111/tra.12524

Weckman, A., A. Di Ieva, F. Rotondo, L.V. Syro, L.D. Ortiz, K. Kovacs, and M.D. Cusimano. 2014. Autophagy in the endocrine glands. *J. Mol. Endocrinol.* 52:R151–R163. https://doi.org/10.1530/JME-13-0241

Wendler, F., L. Page, S. Urbe, and S.A. Tooze. 2001. Homotypic fusion of immature secretory granules during maturation requires syntaxin 6. *Mol. Biol. Cell*. 12:1699–1709. https://doi.org/10.1091/mbc.12.6.1699

Wicksteed, B., C. Alarcon, I. Briaud, M.K. Lingohr, and C.J. Rhodes. 2003. Glucose-induced translational control of proinsulin biosynthesis is proportional to preproinsulin mRNA levels in islet β-cells but not regulated via a positive feedback of secreted insulin. *J. Biol. Chem.* 278: 42080–42090. https://doi.org/10.1074/jbc.M303509200

Xiong, Q.Y., C. Yu, Y. Zhang, L. Ling, L. Wang, and J.L. Gao. 2017. Key proteins involved in insulin vesicle exocytosis and secretion. *Biomed. Rep.* 6: 134–139. https://doi.org/10.3892/br.2017.839

Xue, Y., W. Zhao, W. Du, X. Zhang, G. Ji, W. Ying, and T. Xu. 2012. Ultrastructural study of insulin granules in pancreatic β-cells of db/db mouse by scanning transmission electron microscopy tomography. *Protein Cell*. 3:521–525. https://doi.org/10.1007/s13238-012-2937-1

Yaekura, K., R. Julyan, B.L. Wicksteed, L.B. Hays, C. Alarcon, S. Sommers, V. Poitout, D.G. Baskin, Y. Wang, L.H. Philipson, and C.J. Rhodes. 2003. Insulin secretory deficiency and glucose intolerance in Rab3A null mice. *J. Biol. Chem.* 278:9715–9721. https://doi.org/10.1074/jbc.M211352200

Zhou, Y., Z. Liu, S. Zhang, R. Zhuang, H. Liu, X. Liu, X. Qiu, M. Zhang, Y. Zheng, L. Li, et al. 2020. RILP restricts insulin secretion through mediating lysosomal degradation of proinsulin. *Diabetes*. 69:67–82. https://doi.org/10.2337/db19-0086

Supplemental material

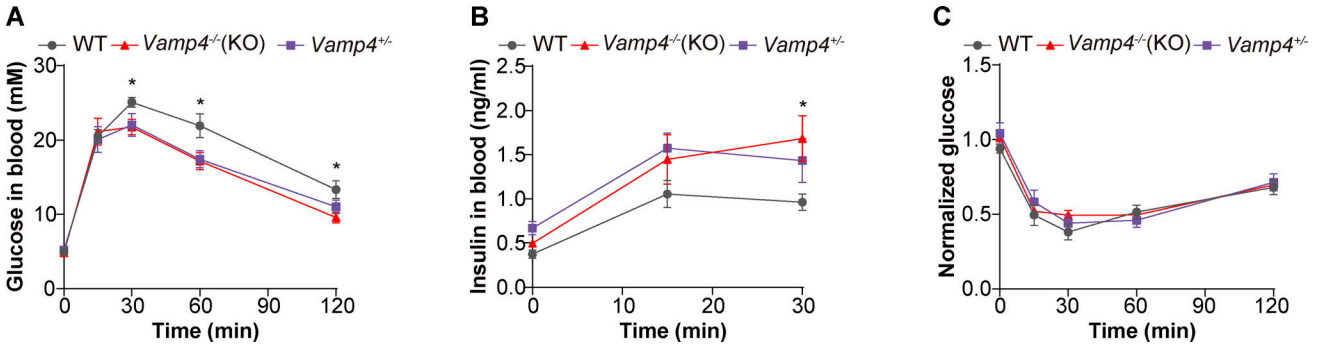

Figure S1. **VAMP4 KO mice exhibit hyperresponsiveness to glucose. (A)** GTT results for male WT mice, homozygotic VAMP4 KO mice (*Vamp4*$^{-/-}$), and heterozygotic VAMP4 KO mice (*Vamp4*$^{+/-}$) at 14 wk of age (n = 6–7 mice per group); 2 g/kg glucose was used in the test. The asterisks indicate WT vs. KO. **(B)** The blood insulin levels in the GTT of male WT mice, homozygotic VAMP4 KO mice (*Vamp4*$^{-/-}$), and heterozygotic VAMP4 KO mice (*Vamp4*$^{+/-}$) at 14 wk of age were measured by ELISAs at 0, 15, and 30 min (n = 6–7 mice per group). The asterisks indicate WT vs. KO. **(C)** ITT results of male WT mice, homozygotic VAMP4 KO mice (*Vamp4*$^{-/-}$), and heterozygotic VAMP4 KO mice (*Vamp4*$^{+/-}$) at 16 wk of age (n = 6–7 mice per group); 0.5 U/kg insulin was used in the test. The data are presented as the mean ± SEM. *, P < 0.05. The statistical analyses were performed with two-tailed unpaired Student's t test (A–C).

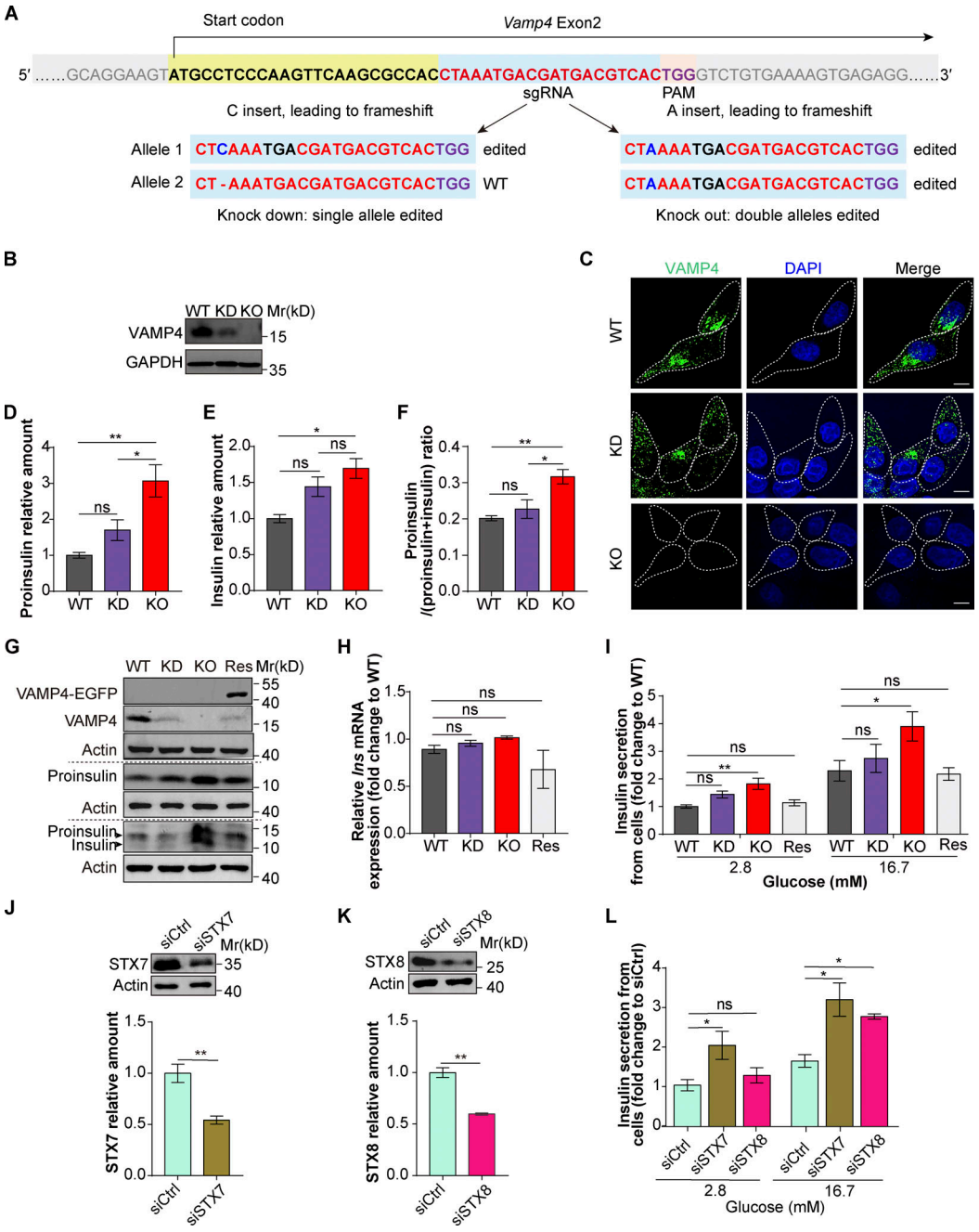

Figure S2. **VAMP4 deficiency causes increases in intracellular (pro)insulin and insulin release. (A)** Schematic diagram of strategies for the generation of VAMP4 gene-edited INS-1 cells using the CRISPR/Cas9 technique. An sgRNA was designed after the start codon of the *Vamp4* gene. A VAMP4 KD cell line in which a single allele was edited and a VAMP4 KO cell line in which double alleles were edited were then obtained. **(B)** Representative Western blot images showing the expression levels of VAMP4 in WT, KD, and KO INS-1 cells (n = 3 biological independent experiments). GAPDH was used as a loading control. **(C)** Representative confocal images of VAMP4 staining (green) in WT, KD, and KO INS-1 cells (n = 3 biological independent experiments). The nuclei of cells were stained with DAPI (blue). Scale bars, 5 µm. **(D and E)** Quantification of the proinsulin levels (D) and insulin levels (E) in WT, KD, and KO INS-1 cells by ELISA (n = 4 biological independent experiments). **(F)** Analysis of the ratio of proinsulin to total insulin (proinsulin and insulin) in WT, KD, and KO INS-1 cells based on data shown in D and E (n = 4 biological independent experiments). **(G)** Representative Western blot images showing the expression levels of VAMP4, proinsulin, and insulin in WT, KD, KO, and rescued INS-1 cells. Actin was used as a loading control (n = 3 biological independent experiments). **(H)** RT–PCR analysis of the *Ins* mRNA levels in WT, KD, KO, and rescued INS-1 cells. *18S* ribosomal RNA was used as an internal control (n = 3 biological independent experiments). **(I)** Measurement of insulin secretion from WT, KD, KO, and rescued INS-1 cells incubated for 1 h in the presence of 2.8 or 16.7 mM glucose (n = 6 biological independent samples). **(J and K)** Representative Western blot images (upper panel) showing the expression levels of STX7 (J) and STX8 (K) in INS-1 cells 72 h after transfection with siRNAs (siCtrl, siSTX7, and siSTX8). The bar graphs (lower panel) show the knockdown efficiency of STX7 and STX8 quantified from three independent Western blot results. Actin was used as the loading control. **(L)** Measurement of insulin secretion from INS-1 cells at 72 h after transfection with siCtrl, siSTX7, or siSTX8. The cells were incubated for 1 h in 2.8 or 16.7 mM glucose. The data are shown as the mean ± SEM (n = 3 biological independent experiments). The data are presented as the mean ± SEM. *, P < 0.05 and **, P < 0.01. The statistical analyses were performed with two-tailed unpaired Student's t test (J and K) and one-way ANOVA (D–F, H, I and L). Source data are available for this figure: SourceData FS2.

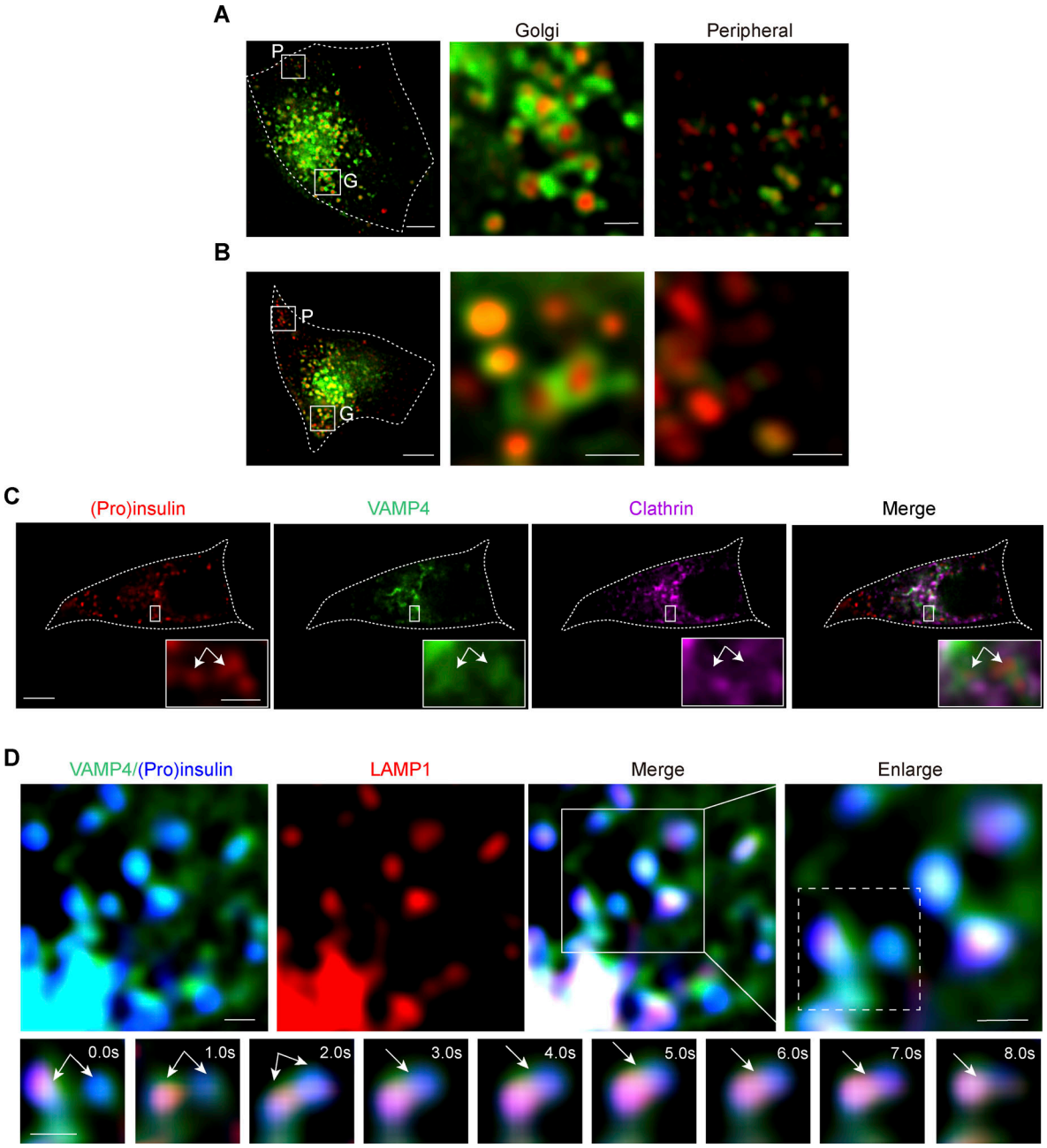

Figure S3. **VAMP4 is packaged into clathrin-coated iISGs near TGNs and VAMP4-positive vesicles fuse with lysosomes. (A and B)** INS-1 cells were transfected with EGFP-tagged VAMP4 (green) and mCherry-tagged (pro)insulin (red; A) or EGFP-tagged VAMP4 (green) and Halo-tagged (pro)insulin (red; B) plasmids for 48 h, and live-cell imaging was performed using the Delta Vision OMX V3 system with 100× (NA = 1.40). Scale bars, 5 µm. The enlarged diagrams indicate the Golgi (G) region and peripheral (P) region. Scale bars, 1 µm. **(C)** INS-1 cells were transfected with EGFP-tagged VAMP4 (green), Halo-tagged (pro) insulin (red), and mCherry-tagged clathrin (magenta) for 48 h, and live-cell imaging was performed using the Delta Vision OMX V3 system with 100× (NA = 1.40). The enlarged images show that VAMP4-positive iISGs colocalize with clathrin (indicated by arrows). Scale bars, 3 µm (left) and 0.5 µm (right). **(D)** INS-1 cells were transfected with EGFP-tagged VAMP4 (green), mCherry-tagged (pro)insulin (blue), and Halo-tagged LAMP1 (red) for 48 h, and live-cell imaging was performed using a Delta Vision OMX V3 system with 100× (NA = 1.40). The diagram and a snapshot of a consecutive event showed that VAMP4-positive vesicles fused with lysosomes (indicated by arrows). Scale bars, 0.5 µm.

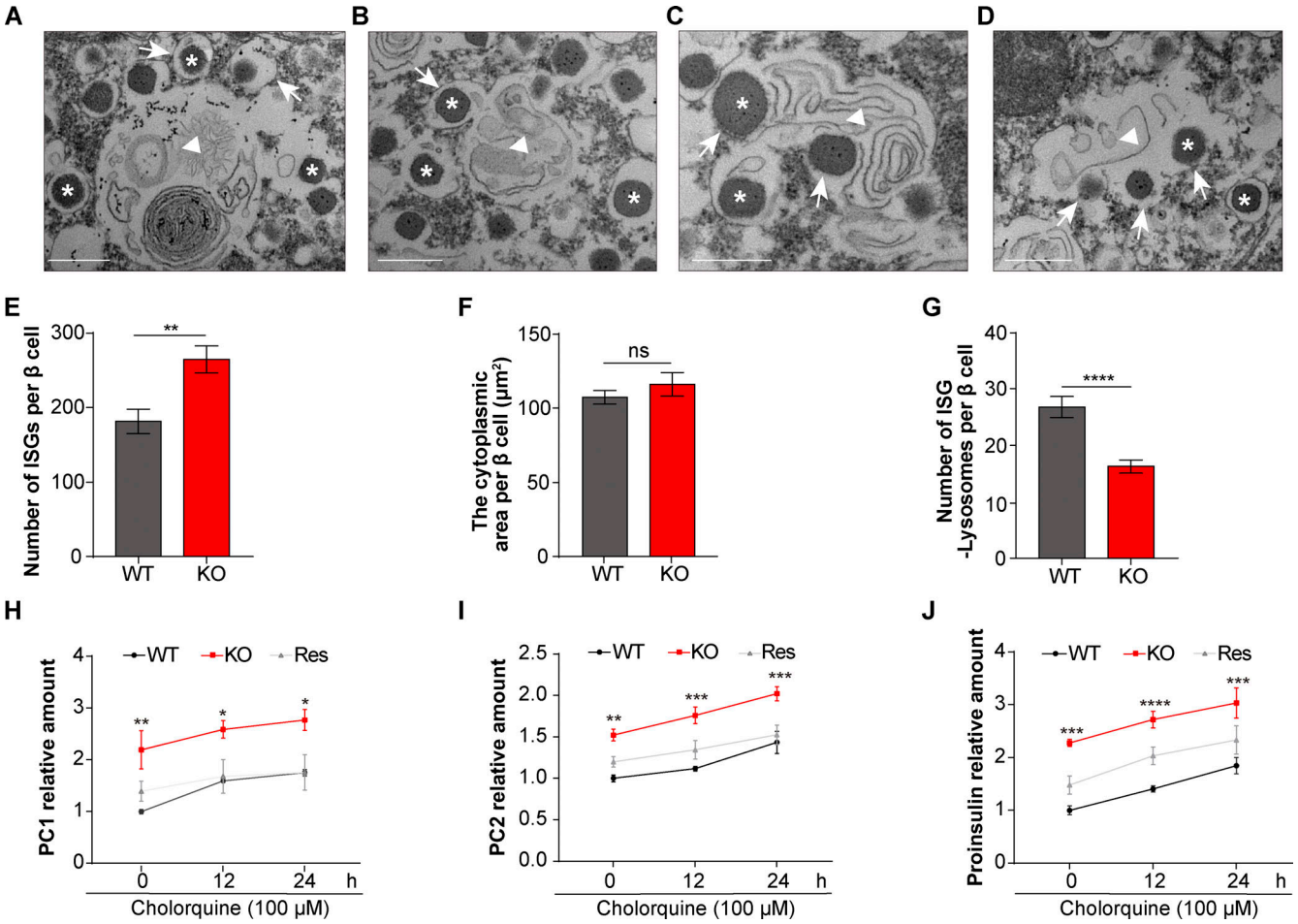

Figure S4. **VAMP4 facilitates the fusion of iISGs and resorted vesicles with lysosomes for granule cargo degradation. (A–D)** The state of ISG-lysosome contact events (A), ISG-lysosome fusion events (B), ISG-lysosome engulfment events (C), and ISG-lysosome degradation events (D) were observed in the region of interest in EM images of pancreatic β cells from WT mice (indicated by arrows). The EM images were captured at 120 kV and a magnification of 23,000×. Triangle: lysosome; asterisk: ISG. Scale bars, 0.5 μm. **(E–G)** The number of ISGs per β cell (E), cytoplasmic area of β cells (F), and number of ISG-lysosome interactions (G) in β cells of the WT and KO mice were quantified from EM images shown in Fig. 7 A. **(H–J)** Line charts showing the expression levels of PC1 (H), PC2 (I), and proinsulin (J) quantified as fold changes with respect to the average values measured at 0 h for the WT based on the Western blot bands shown in Fig. 7 H (n = 3 biological independent experiments). The data used for the analyses in E–G were based on 25 β cells in two islets isolated from one WT male mouse and 24 β cells in three islets isolated from two VAMP4 KO male mice. The WT and KO mice were 16 wk of age. The data are presented as the mean ± SEM. *, P < 0.05; **, P < 0.01; ***, P < 0.001; and ****, P < 0.0001. The statistical analyses were performed with two-tailed unpaired Student's t test (E–G) and two-way ANOVA (H–J).

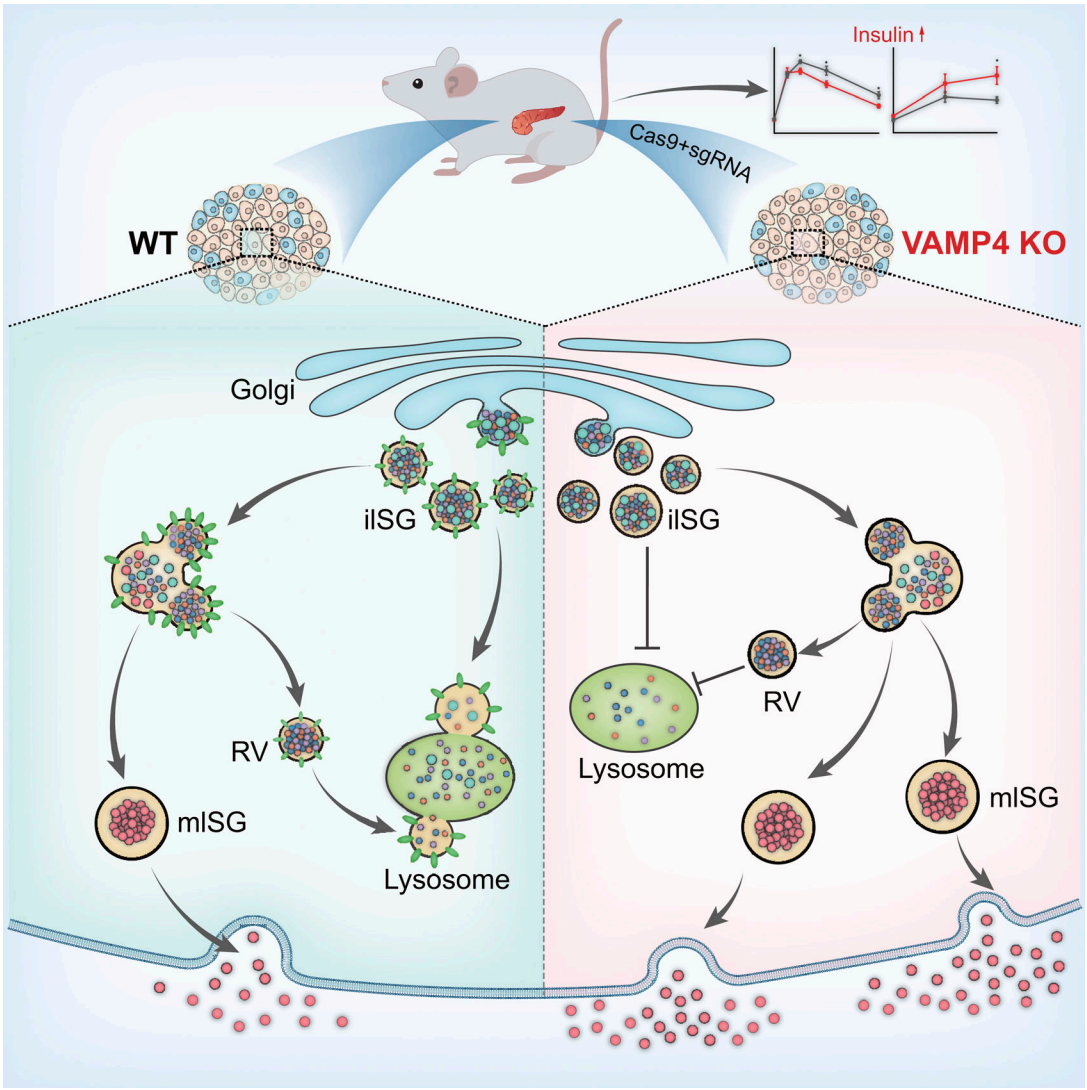

Figure S5. **VAMP4 regulates the insulin levels by facilitating the membrane fusion of iISGs and resorted vesicles with lysosomes.** Working model illustrates that VAMP4 acts as a key regulator for the control of insulin quantity and quality. Briefly, VAMP4 KO mice exhibit hyperresponsiveness to glucose due to increased blood insulin levels in response to glucose challenge. VAMP4-deficient pancreatic β cells show an accumulation of intracellular insulin, an increase in insulin release, and an elevated proportion of immature proinsulin. Mechanistically, in β cells, VAMP4 is packaged into iISGs at TGNs, and partial VAMP4-positive iISGs directly fuse with lysosomes via crinophagy. VAMP4 can also be resorted to vesicles and removed from iISGs by membrane remodeling during granule maturation, and VAMP4-positive resorted vesicles subsequently fuse with lysosomes. VAMP4 forms a SNARE complex with STX7, STX8, and VTI1B on lysosomes and promotes the membrane fusion of iISGs and resorted vesicles with lysosomes, which ensures the breakdown of excess (pro)insulin and obsolete materials to maintain intracellular insulin homeostasis. VAMP4 deficiency not only blocks the fusion of iISGs with lysosomes, causing the accumulation of numerous iISGs and some blocked iISGs swarming to the maturation and secretion pathway, but also blocks the fusion of VAMP4-positive resorted vesicles with lysosomes, leading to undesired cargo material accumulation. RV, resorted vesicle.

Video 1. **Intracellular trafficking of VAMP4-positive vesicles and insulin granules in vivo.** VAMP4-positive vesicles and insulin granules were labeled with EGFP-tagged VAMP4 (green) and mCherry-tagged (pro)insulin (red), respectively. The two plasmids were simultaneously transfected into INS-1 cells. 48 h after transfection, live-cell imaging was performed at 37°C in an atmosphere with 5% CO_2 using a Delta Vision OMX V3 system in the wide-field mode with an exposure time of 0.01 s at each frame and an interval time of 0.5 s for 1.7 min. The playback speed of video was 30 frames per second. The movie shows that VAMP4 localizes to iISGs at the Golgi regions but disappears on mISGs in the peripheral regions (indicated by arrows), which reveals that VAMP4 is budded and removed from iISGs during membrane remodeling of granule maturation.

Video 2. **Intracellular trafficking of VAMP4-positive vesicles and lysosomes in vivo.** VAMP4-positive vesicles and lysosomes were labeled with EGFP-tagged VAMP4 (green) and mCherry-tagged LAMP1 (red), respectively. The two plasmids were simultaneously transfected into INS-1 cells. 48 h after transfection, live-cell imaging was performed at 37°C in an atmosphere with 5% CO_2 using a Delta Vision OMX V3 system in the wide-field mode with an exposure time of 0.01 s at each frame and an interval time of 0.5 s for 1 min. The playback speed of video was 30 frames per second. The movie shows that VAMP4-labeled signals fuse with lysosomes and diffuse on the lysosomal membrane (indicated by arrows), which reveals that VAMP4-positive vesicles are transported to and fuse with lysosomes.

Video 3. **Intracellular trafficking of insulin granules and lysosomes in vivo.** Insulin granules and lysosomes were labeled with mCherry-tagged (pro)insulin (red) and Halo-tagged LAMP1 (green), respectively. The two plasmids were simultaneously transfected into INS-1 cells. 48 h after transfection, live-cell imaging was performed at 37°C in an atmosphere with 5% CO_2 using a Delta Vision OMX V3 system in the wide-field mode with an exposure time of 0.01 s at each frame and continuous sampling for 0.75 min. The playback speed of video was 30 frames per second. The movie shows partial (pro)insulin-labeled iISGs directly fuse with lysosomes (indicated by arrows).